Johannes Stemsrud

De-Icing Coatings Based on Solar Illumination

Preparation and characterization

Masteroppgave

NTNU
Kunnskap for en bedre verden

Johannes Stemsrud

De-Icing Coatings Based on Solar Illumination

Preparation and characterization

NTNU
Kunnskap for en bedre verden

De-Icing Coatings Based on Solar Illumination

Author:

Johannes Stemsrud

Preface

The work performed in this report is performed by Johannes Stemsrud, from January 2023 to November 2023 as a part of the course TMT4910 - Nanotechnology, Master's thesis. The laboratory work and the guidance meetings were done at the Department of Materials Science and Engineering (IMA) at the Norwegian University of Science and Technology (NTNU) in Trondheim. Professor Hilde Lea Lein has been the supervisor and Ph.D. candidate Michael Robert Kelly has been the co-supervisor.

Acknowledgements

Abstract

De-icing a surface is important for a variety of different structures in colder climates, like roads, powerlines, windmills, or in the aviation industry. The objective of this work was to investigate the fabrication process and characterize four different coatings designed for de-icing surfaces. The coatings consist of three layers, which together acts as a photothermal trap. The surface layer acts as an absorber, the second layer acts as a heat spreader and the third and final layer acts as an insulating layer. By using light only, this method of de-icing surfaces is considered to be more environmentally friendly than the more traditional active de-icing methods like electrical heating or using chemical solutions.

The absorber layer is considered to be the crucial layer in a photothermal trap. It absorbs incoming radiation and converts it to thermal energy. It is also the layer exposed to the surroundings. In this project, prototype coatings of four different absorber layers were fabricated. Three coatings consisted of both the ceramic powders SiC and CuO, while one coating consisted of only SiC as the absorbing material. The ceramic powders were mixed with polyvinyl butyral as the binder, and ethanol as the solvent. The slurries were then cast onto the aluminum foil with a tape caster to make the top two layers of a photothermal trap.

The de-icing properties were characterized using a variety of different experimental setups inside a styrofoam box where frozen droplets were illuminated and the melting time was measured. The surface properties were characterized with scanning electron microscopy (SEM). The wetting properties were characterized with a drop shape analyzer using the water contact angle (WCA). The durability was tested with a micro scratch test.

The four prototype coatings with de-icing effects were successfully fabricated. The durability characterization revealed a strong coating for the 75/25 SiC/CuO prototype. The wetting characterization showed most coatings to be hydrophilic, except for the 75/25 SiC/CuO prototype, which had a hydrophobic nature. The de-icing characterization proved all prototypes to have de-icing properties under illumination. The coating consisting of 75/25 SiC/CuO proved to be the most durable, has a hydrophobic surface and a quick de-icing time, and is therefore the prototype recommended as the absorber layer in a photothermal trap.

Sammendrag

Avising av overflater er viktig for ulike strukturer i kaldt klima, som veier, høyspentlinjer, vindmøller eller i luftfartsindustrien. Målet med dette arbeidet er å undersøke fabrikasjonsprosessen og karakterisere fire ulike belegg med avisende effekt. Beleggene består av tre lag med egenskapene til en fototermisk felle. Det øverste laget absorberer, det andre laget sprer varme, og det siste laget isolerer. Ved å kun bruke lys er denne metoden sett på som mindre skadelig for naturen enn de mer tradisjonelle aktive avisingsmetodene, som elektrisk varme eller kjemiske løsninger.

Det absorberende laget er det viktigste laget i en fototermisk felle. Dette laget absorberer inkommende stråling og omformer det til varmeenergi. Det er også eksponert til omverdenen. Prototyper av belegg med fire ulike absorberende lag ble laget. Tre av beleggene består av en blanding av både SiC og CuO, og ett av beleggene består kun av SiC. De keramiske pulverene ble blandet med polyvinyl butyral som bindemiddel og etanol som løsemiddel. Disse ble så støpt på aluminiumsfolie ved hjelp av keramisk båndstøping.

De avisende egenskapene ble karakterisert med et enkelt eksperimentelt oppsett i en kjøleboks hvor fryste dråper ble belyst og smeltetiden ble målt. Overflateegenskapene ble karakterisert med sveipeelektronmikroskopi (SEM). Mekanisk motstandsevne ble karakterisert med skrapetesting. Fuktegenskapene ble karakterisert med vannkontaktvinkelmåling.

Fabrikasjonen av de fire beleggprototypene med avisende effekt var vellykket. Den mekaniske motstandsevnen viste at belegget med 75/25 SiC/CuO var sterkest. Karakteriseringen av fuktegenskapene viste at alle beleggene hadde hydrofile egenskaper, utenom 75/25 SiC/CuO som hadde hydrofobe egenskaper. Karakteriseringen av avisingen viste at alle prototypene hadde avisende effekt under belysning. Belegget med 75/25 SiC/CuO var det sterkeste, hadde hydrofobisk overflate og rask avisiende tid, og er derfor det som er anbefalt til bruk i det absorberende laget i en fototermisk felle.

List of abbreviations and symbols

1. **BSE**: Backscattered electrons

2. **DSA**: Drop shape analyzer

3. **EtOH**: Ethanol

4. **MST**: Micro scratch test

5. **PSD**: Particle size distribution

6. **PVB**: Polivinyl butyral

7. $\mathbf{R}_a$: Arithmetical rougness

8. **SEM**: Scanning electron microscopy

9. **SiC**: Silicon carbide

10. **WAF**: Water adhesion foce

11. **XRD**: X-ray diffraction

12. θ : Contact angle

Table of Contents

1   Background

De-icing is important in many industries that operate in colder climates. Airplanes lose their aerodynamics properties and become heavier with the formation of ice on their surfaces. Solar cells will absorb less light if a layer of ice is formed on its surface. Windmills will produce less power if ice is formed on their blades. Some wind turbines have reported a loss of 50 percent in production rate due to ice formation [1]. These are examples of unfortunate results of the formation of ice in a variety of industries. Other problems which may be more often encountered day-to-day are slippery roads and heavy power lines.

There are different ways of dealing with ice and many of the methods used today tend to be environmentally unfriendly. Extensive use of glycols and salts are used for de-icing in the aviation sector [2]. These chemicals can be environmentally harmful to surrounding areas. Windmills tend to use the produced power to heat their outer surface to prevent ice from forming. Reducing the required energy used for de-icing will lead to more efficient green energy production. The increased focus on green energy and environmentally friendly systems has led to a great amount of research on new green methods for de-icing surfaces.

1.1   Ice mitigation tactics

Anti-icing and de-icing are two terms often used when considering surface icing. Anti-icing methods focus on preventing ice from forming, while de-icing methods are methods that remove ice which has already been formed. The de-icing methods are often active, meaning they require energy to remove the ice. Such methods can be electrical heating of the substrate, as is done for windmills operating in colder climates. A more traditional active de-icing method is mechanically removing ice by hammering, scraping, or physically breaking it. This can however damage the underlying surface over time.

A method which can be used both as a de-icing method, and an anti-icing method is the introduction of chemical solutions which lower the freezing point of the substrate. An example of this method is in the aviation industry where they use chemical solutions with salts and glycols to remove ice and make a coating with anti-icing properties. These chemicals are however harmful to the surrounding environment[3].

Thermally heating the surface of the substrate is one of the more common active anti- and de-icing methods used today. It is based on using thermal heat to prevent ice formation or to melt ice which has already been formed. Although it is possible to use green energy to thermally heat objects, the process itself is energy-intensive. Windmills placed in colder climates have reported using up to half of the produced power only to heat its surface to prevent ice formation on the blades [1]. These methods are examples of different strategies used today when trying to prevent or remedy the formation of ice. They are effective against ice, but tend to be either harmful to the substrate, environmentally unfriendly, energy-intensive or expensive[4].

Passive methods, on the other hand, do not require an external energy source other than natural forces like solar radiation and wind. Recent studies have looked into changing the microstructure of the surface on a coating like amphiphilic and icephobic coatings where the surface contains both hydrophilic and hydrophobic components[5]. One of the more challenging aspects of passive coating solutions is their durability. Many of the structures that need de-icing surfaces are exposed to extreme weather conditions, and thin coatings wear down quite fast in such harsh environments[6]. Recent studies have for this reason studied coatings that can be more mechanically robust, while simultaneously inhibit de-icing properties[7, 8].

The use of hydrophobic surfaces is a complex matter for de-icing surfaces. There is plenty of research on hydrophobic and superhydrophobic surfaces for icephobic purposes. There is, however, not yet a correlation between icephobicity and hydrophobicity [9, 10]. Even without a clear correlation, there are areas where hydrophobic surfaces can be considered beneficial for de-icing. An example is that droplets fall off hydrophobic surfaces more easily than hydrophilic surfaces, which is favorable if the substrate is dependent on sunlight for heating. The ice that melts will turn into water that quickly glides off the surface. For de-icing methods, hydrophobic surfaces work as a self-cleansing aspect of the coating [11].

This leads up to the more recent field of de-icing coatings. We need a de-icing surface that is durable, cheap, efficient, and uses clean energy. The photothermal trap can mark off most of these criteria and might be the future of de-icing coatings.

1.2   Photothermal trap

Figure 1.1 shows an overview schematic of a photothermal trap [4]. The trap utilizes illumination to produce thermal heat and concentrates the heat just at the surface of the substrate. It consists of three layers interacting together to absorb light, spread heat, and insulate to prevent heat loss to the substrate. The top layer is the absorbing layer, colored dark purple in Figure 1.1. This layer is the crucial layer in the coating when it should consist of a selective absorber that absorbs a major fraction of the incoming radiation as well as being a durable material because of its location on the surface of the substrate. It should also have hydrophobic properties to remove melted ice quicker and become self-cleaning.

The second layer is the thermal spreader. Incoming illumination can vary, due to shadowing, angles to the incoming radiation, and already existing surface ice. Adding a material with high thermal conductivity in the photothermal trap will make the heat spread out to potentially unexposed areas of the coating. This is the thought behind the second layer; the thermal spreader layer, colored orange in Figure 1.1. This layer should consist of metals like aluminium which has a high thermal conductivity.

The third and final layer is the insulating layer, colored gray in Figure 1.1. This layer is in place to reduce heat loss into the base of the substrate. The insulating layer makes the coating concentrate the produced heat just at the surface, which is important to make a more efficient photothermal trap for de-icing surfaces.

The three layers combined can cause an increase in temperature at the coating surface potentially melting a layer of already-formed ice at the ice/coating interface. This creates a slippery water film between the ice and the coating which lowers the ice adhesion. This can make accumulated ice slide off easier, in turn making the surface more exposed to incoming light. This is, as mentioned above, the reason why the research community has focused on hydrophobic surfaces and self-cleansing coatings[11]. Using a hydrophobic surface can make the ice glide off earlier at the ice/coating interface when a water film is present.
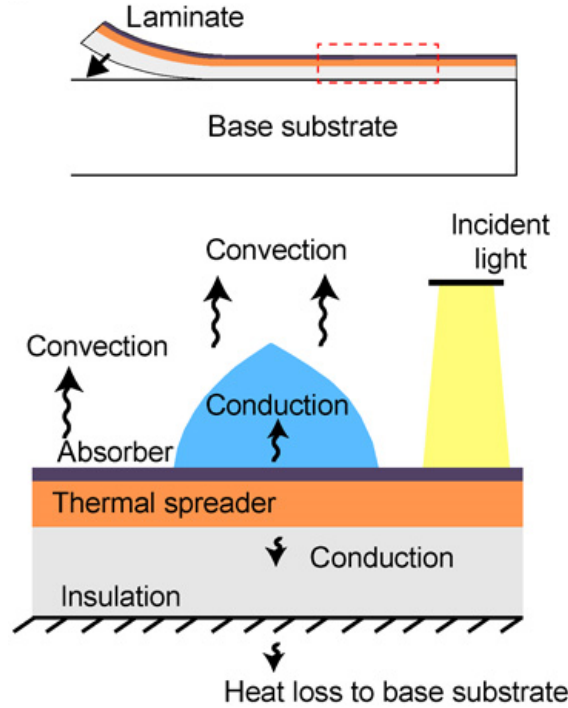
Figure 1.1: Illustration of how a photothermal trap is structured, as well as how heat spreads when the photothermal trap is illuminated (From Science Advances© Dash, de Rutier, Varanasi [4]). In this report, SiC and a mixture of SiC and CuO are used in the absorber layer. A 50 µm thick aluminum foil is used as the thermal spreader layer.

1.3   Aim of the work

The aim of this Master's thesis is to fabricate four prototype coatings with de-icing properties. The coatings use illumination to absorb incoming radiation and generate heat to melt any accumulated ice on its surface. They consist of the two top layers of a photothermal trap, namely the absorber layer and the thermal spreader layer. The absorber layer is different for the four prototypes, while the thermal spreader layer stays the same for all the prototypes. One of the prototypes has an absorber layer consisting of SiC and latter three prototypes have absorber layers consisting of three different mixtures of SiC/CuO. The thermal spreader layer consists of aluminum.

The thesis is an extension of the work performed by the author in the specialization project[12].

The four different coatings are characterized by their de-icing properties. The particle size and surface morphology are characterized using a Partica La-960 and a SEM respectively. The mechanical properties and durability of the coatings are investigated for industrial purposes using a micro-scratcher. The water contact angle is measured to indicate their hydrophobicity to make a slippery and self-cleaning surface. Their de-icing characteristics are investigated using an experimental setup with a cold chamber and a source of light, explained further in the experimental section.

The final aim is to determine which of the prototypes is best suited as the absorber layer in a photothermal trap.

2   Introduction

2.1   Icing

The formation of ice on surfaces happens wherever the temperature is below zero and water is present and depends on the electrostatic forces at the solid-ice interface [13]. Ice can come in different forms like snow, glaze, rime, and frost. Snow, glaze, and rime all go from liquid to solid in the phase transition, while frost is the only type of ice that can form directly from water vapor. The ice molecules are held together by hydrogen bonds and the lattice forms a hexagonal structure with some variations due to disorder in the crystals[14].

Atmospheric icing is a term used for all types of accretion of ice[15], and can be further divided into two main groups, namely (1) precipitation icing, and (2) in-cloud icing. Both may cause problems for industries operating in freezing climates. Such icing often happens around circumpolar regions, high altitude regions, or any place where snow exists or temperatures drop below the freezing point of water.

Precipitation icing is often linked to wet snow and freezing rain, but can also cause glaze. It depends on variations in temperature and the altitude. It can occur in any place where a combination of precipitation and freezing temperatures are in place.

In-cloud icing is often linked to soft and hard rime. It can only occur in clouds that consist of supercooled droplets. Supercooled droplets are droplets that remain liquid below the freezing point of water. Depending on the temperature, the size distribution of the cloud droplets, the liquid water content, and the wind speed, soft or hard rime may form. These conditions are often met at the top of mountains and are causing problems for windmills and telecommunication towers.

Icephobicity is the ability of a material to repel ice or ice formation. Ice adhesion strength is defined as the maximum force per unit area needed to remove ice [16]. Materials with low ice adhesion are therefore preferable in the fields where icing is a problem. In the pursuit of materials with icephobic properties, recent studies have reported anti-icing behavior for superhydrophobic surfaces [17][18]. There are however other characteristics that might influence the freezing delay, like the surface roughness and its effect on ice nucleation and nuclei growth [19]. Historically iceph-obicity has been closely linked to hydrophobicity, but this is an outdated theory and is not unanimous among researchers. A hydrophobic surface can however be bene-ficial to a photothermal trap considering the potential self-cleaning properties[11]. This is further explained in the next chapter. Icephobicity remains a complex topic and the perfect icephobic material is yet to be discovered[20].

2.2   Wetting

One of the most important factors when it comes to investigating water in contact with a material is the wettability of the material. When considering ice, the water contact angle (WCA) is related to the ice adhesion in the way that having a small

water contact angle gives a high ice adhesion[21]. The WCA is the angle formed tangential to the water droplet at the air–liquid–solid interface, as shown in Figure 2.1. Hydrophobic materials have WCAs of more than 90° and hydrophilic materials have WCAs smaller than 90°.
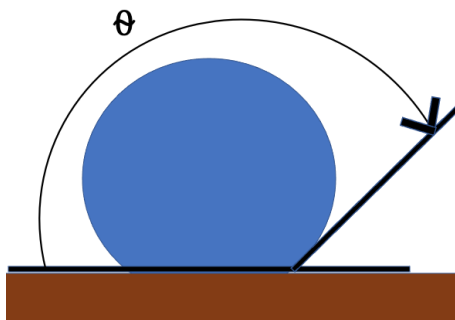

Figure 2.1: Illustration of a water droplet on a surface and the water contact angle, θ, between the droplet and the surface.

The WCA can easily be measured using a drop shape analyzer. Such an instrument deposits a droplet and uses a camera to measure the water contact angle.

The wetting of surfaces is often described by one of two models[22, 23]. One of them is the Wenzel model which takes the pores along the surface of the material into consideration. It assumes the liquid in contact with a surface will fill all the pores completely. It thereby says that a rough surface will increase the liquid-solid interface surface, and therefore a hydrophobic material will experience increasing contact angles with increasing surface roughness.

Jamil et al.[11] reported outstanding deicing surfaces in their slippery photothermal trap, due to the infusion of silicone oil into the surface nanostructures and thereby creating a hydrophobic surface. A hydrophobic surface is beneficial for the photothermal trap in the way of being self-cleaning. When the first ice melts and creates a film of water between the surface and the accumulated ice, the hydrophobic surface makes the ice slide off the surface faster than a hydrophilic surface. This is crucial to have ice melting and removal happening faster than ice buildup, thus preventing further ice accumulation.

2.3   Mechanical properties

The micro scratch test method is a method used to determine the adhesive strength and scratch resistance of the coating-substrate system[24]. This can be used to get a better understanding of the durability of the absorber layer. Investigating the mechanical properties of the coating is of importance for de-icing coatings because the structures that need de-icing coatings tend to be exposed to extreme weather conditions, and these thin coatings wear down quicker in these conditions[6]. A durable coating is essential to make the prototypes commercially available.

The micro scratch test generates a scratch using a diamond indenter (usually a Rockwell C profile). The indenter is drawn across the surface with constant or progressively increasing load at a constant speed. The scratch can penetrate and damage the coating at a certain load. This load value is the critical load, L_c, which can be used to characterize the adhesive strength of the coating-substrate system.

2.4   Coating deposition technique

The term casting is often linked to metal casting in which a shape is formed by pouring metal into a mold at high temperatures, however, the casting of ceramics is more frequently done at lower temperatures. In room-temperature operations where ceramic particles suspended in liquid are cast into a porous mold, the liquid is removed and leaves a specific structure in the mold. There are many variations to this process, depending on the final particulate compact, the ceramic liquid suspension and the procedures used. The ceramic absorber layer in a photothermal trap has to be quite thin and the fabrication process has to be cheap. The tape casting method has been developed to fabricate thin sheets in large quantities and at low cost, which makes it a fitting casting method for this application.

Tape casting is a common casting method used to fabricate a thin layer of a coating material consisting of a ceramic slurry. The doctor blade process is the most common tape casting approach [25]. This approach includes the deposition of a coating material in front of a blade with a fixed height. The coating material is cast onto a moving carrier surface and the slurry is spread to a specific thickness chosen by the height of the doctor blade. Alcohols can be used as the solvent for such slurries. Some doctor blade processes use heat to dry the coating after the casting, but by using alcohol the coating is dried by evaporation and no external heat is needed. This method can be used to make thin sheets in large quantities and at low cost.

2.5   De-icing

There are different ways to characterize the performance of de-icing materials and there is, to this date, no standardized setup utilized by researchers. The humidity, airflow, and temperature need to be kept constant when characterizing the de-icing properties of a coating inside a chamber. Illumination is a key variable for de-icing in a photothermal trap, which complicates the de-icing characterization setup. Sources of illumination often radiate varying amounts of thermal energy which can lead to increasing temperatures surrounding the substrate. Dash et al. [4] studied the de-icing properties of their photothermal trap using a cold chamber with a side viewport. A halogen fiber light with low thermal radiation was used to keep the temperature sub-zero. With this setup, they managed to keep low and constant temperatures while simultaneously recording the coating surface through the side viewport. This setup is expensive and complex and the following paragraphs look into an alternative setup using no side view port.

In 2014 former NTNU student Raasok wrote their Master thesis on hydrophobic anti-

icing coatings [26] and used a simple experimental setup. A 45° inclined aluminum plate was cooled to sub-zero temperatures in a walk-in freezer. The coatings were mounted to the plate and finely dispersed water was sprayed onto the coatings. The freezing behavior of the dispersed water was monitored as well as the subsequent melting behavior. This experimental setup was inspired by Lee et al. [27].

The photothermal trap is dependent on a light source and it is of interest to experiment with no illumination as well as with illumination to see the effect of lighting alone. Capturing the melting behavior of droplets with a camera when there is no light is however problematic. Earlier studies using the same setup as Raasok have dealt with this problem by having two rows of samples mounted to the aluminum plate and covering one of the rows up [7][8]. A challenge using this method is to measure the melting time. With the prototypes being covered, they could not see when the droplets melted. Using a small light source that gives just enough light to make a camera able to capture the melting behavior would solve this problem. There are therefore two separate experiments conducted; one with a 1050 lm light bulb mounted 10 cm from the prototypes, and one using a small LED light that gives just enough light for the camera to capture the melting behavior of the frozen droplets.

2.6 Material selection

2.6.1 Silicon carbide and cupric oxide

The absorber layer is crucial in the photothermal trap, and the material selection in this layer is important for the overall efficiency of the trap. Some key properties are of importance when choosing the specific material for an absorber layer in a photothermal trap. Absorbtivity, emissivity, thermal conductivity, toxicity, abundance, and cost are some of the important properties to consider when choosing a material for the absorber layer. SiC is a fitting material for this application based on its material properties. It has high thermal conductivity, low toxicity, low cost, absorbs light well, high mechanical strength and is an abundant material.

Earlier studies using the same fabrication process have tested the photothermal de-icing properties of CuO, SiC, and TiN as the materials in the absorber layer[7][8]. These studies showed overall preferable results for the prototypes consisting of SiC, while one of the studies showed promising surface properties for the prototype consisting of CuO[7]. This study also showed a higher optical absorbance when using CuO compared to SiC. CuO is an earth-abundant, nontoxic, high absorption coefficient, and low band-gap material that makes it a fitting material for this application.

The introduction of both SiC and CuO together can increase the absorption of photonics up to 62.2%[28]. A combination of the material properties of SiC and the high absorbance of CuO will be investigated in this study with one prototype consisting of SiC, and three prototypes with different concentrations of SiC and CuO combined.

3 Experimental

The experimental work done in this Master's thesis is summarized and presented in Figure 3.1. Four prototypes were made following the steps shown in the flowchart. The first step is also the shorter step where the two raw powders of ceramic SiC and CuO nanopowder are characterized using SEM. The second step includes all the handling of the slurries, from the mixing of the powders to the final tape casting. The third and final step includes all the characterization methods used to characterize the four coatings.
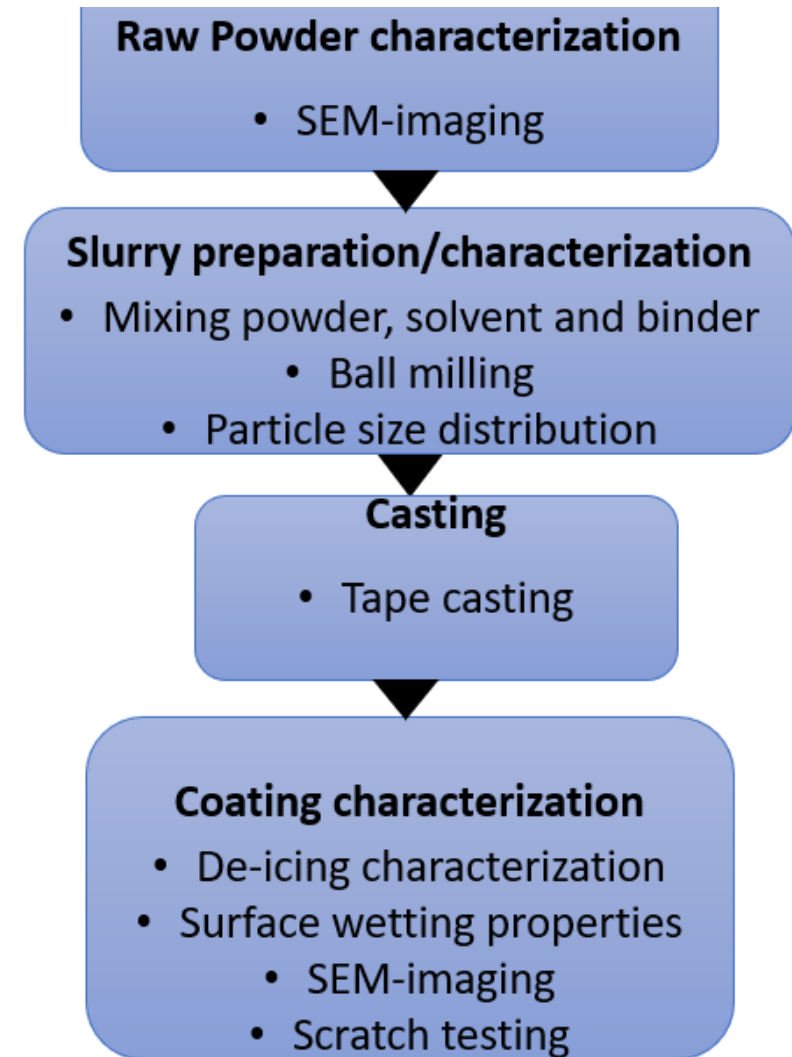

Figure 3.1: Flowchart of the experimental work.

3.1 Chemicals

The two raw powders used for this experiment are silicon carbide (SiC) raw powder bought from *Fiven* and cupric oxide (CuO) raw powder bought from *Sigma Aldrich*. The raw powders were studied using a *Hitachi S3400-N* scanning electron

microscope (SEM) with a secondary electron detector. A droplet of ethanol was deposited onto a 1x1cm aluminum foil piece, and the powders were sprinkled onto the ethanol. After the ethanol evaporated and the powders were sticking to the foil, they were mounted to a SEM sample stub with a piece of carbon tape. The accelerating voltage was set to 10.0 kV for the SiC raw powder and 20.0 kV for the CuO powder. The working distance was set to 4.9mm for the SiC raw powder and 4.3mm for the CuO raw powder.

3.2 Prototype preparation

Four different prototypes were made. The binder- and solvent content were held constant for all prototypes, while the concentration of ceramic powders was changed. One prototype consisted of SiC as the only ceramic powder, while the last three prototypes consisted of a mixture of SiC- and CuO ceramic powders.

SiC: Prototype containing SiC powder as the only ceramic powder.

95/5: Prototype containing 95 mol% SiC- and 5 mol% CuO ceramic powders.

75/25: Prototype containing 75 mol% SiC- and 25 mol% CuO ceramic powders.

50/50: Prototype containing 50 mol% SiC- and 50 mol% CuO ceramic powders.

From this point on, the prototypes will be referred to by the numbers in bold, except for SiC which is called by its name.

Table 1 shows what chemicals, their function, and the amount of each for the SiC prototype.

Table 1: Overview of chemicals in SiC prototype.

Chemical	Function	Amount [g]
SiC	Ceramic powder	30.23
EtOH	Solvent	41.23
PVB	Binder	4.06

Table 2 shows what chemicals, their functions, and the amount of each for the 95/5 prototype.

Table 2: Overview of chemicals in 95/5 prototype.

Chemical	Function	Amount [g]
SiC	Ceramic powder	28.72
CuO	Nanopowder	1.51
EtOH	Solvent	41.23
PVB	Binder	4.06

Table 3 shows what chemicals, their functions, and the amount of each for the 75/25 prototype.

Table 3: Overview of chemicals in 75/25 prototype.

Chemical	Function	Amount [g]
SiC	Ceramic powder	22.68
CuO	Nanopowder	7.56
EtOH	Solvent	41.23
PVB	Binder	4.06

Table 4 shows what chemicals, their functions, and the amount of each for the 50/50 prototype.

Table 4: Overview of chemicals in 50/50 prototype.

Chemical	Function	Amount [g]
SiC	Ceramic powder	15.12
CuO	Nanopowder	15.12
EtOH	Solvent	41.23
PVB	Binder	4.06

The preparation method for the four prototypes was the same and equal to that described in the author's technical report [12]. A 250 mL wide-necked plastic bottle was approximately 1/3 filled with yttrium-stabilized zirconia (YSZ) balls of 3mm. The binder and ceramic powders were measured separately before the solvent of ethanol was measured, to prevent the ethanol from being exposed to air over time. The ethanol was measured in a beaker. The bottle, the powders, and the beaker were put under a fume hood. Then approximately half of the solvent was poured into a beaker on a magnet stirrer. The magnet stirrer was turned on and the binder was slowly poured into the beaker. After the binder was fully mixed with the solvent, the ceramic powder was slowly poured into the mixture. Approximately half of the solvent was spared and used to rinse out the remaining binder and ceramic powder from the plastic boxes they were measured up in. This whole procedure was done as fast as possible to prevent the alcohol from evaporating extensively and let water into the slurry.

After the powders were mixed with all the solvents, the slurry was poured into the plastic bottle with the YSZ-balls. To have enough friction between the surface of the plastic bottle and the ball mill, the bottle was put inside a small nitrile glove before it was left overnight (approx. 18 hours) on a Witeg Ballmill at 155 rpm.

3.3   Tape Casting

The slurry was milled down overnight and then strained from the milling balls, shown in Figure 3.2
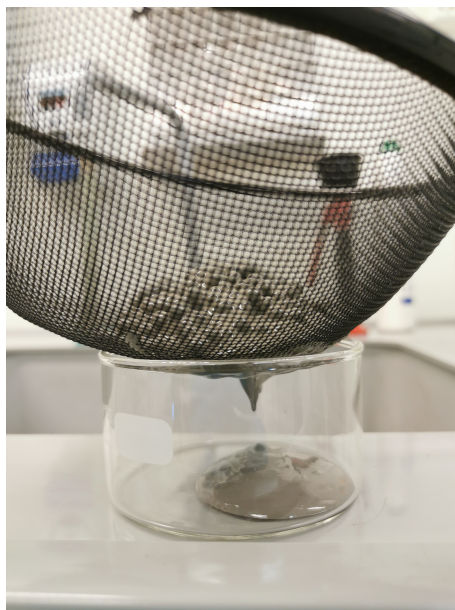
Figure 3.2: Image of the slurry after ball milling being strained.

Using a *Richard E. Mistler DCX Plus* tape caster with a Mylar film, the slurries were cast with a thickness of $50\,\mu m$ onto pieces of aluminum foil. The aluminum foil was $50\,\mu m$ thick and cut into rectangular pieces of approximately 8x25cm beforehand. The aluminum pieces were then flattened by pressing them inside a book, and then using a ruler to scratch along the edges in order to remove any pointy ends. This is to prevent ripping during the casting process. A paper with ethanol was used to clean both sides of the foil, as well as the film on the tape caster.

A 15 cm *Dr.blade* reservoir was used to set the right thickness for the coating. A pre-measured $50\,\mu m$ pin was used to measure the right height for the blade by observing that it fits under the blade at both sides of the aluminum foil and in the middle. This will however scratch up the aluminum foil underneath the blade, and it is therefore necessary to use one piece of aluminum foil to set the right height on the blade, and a new piece of aluminum foil for the actual sample. After the height was set the 8x30 cm aluminum foil which was flattened and cleaned, was taped to the Mylar film on the tape caster. The blade was placed over it, as shown in the Figure 3.3. The maximum speed of the tape caster is 50.8 cm/min. The speed was set to 15 cm/min (30 percent of maximum speed). The coated aluminum pieces were left in the tape caster overnight to dry. Then the 30cm aluminum strips were cut into smaller samples of around 4x4cm. This was done for all of the four prototypes. One set of samples of 1x1cm was cut out and weighed together with a 1x1cm aluminum piece with no coating.
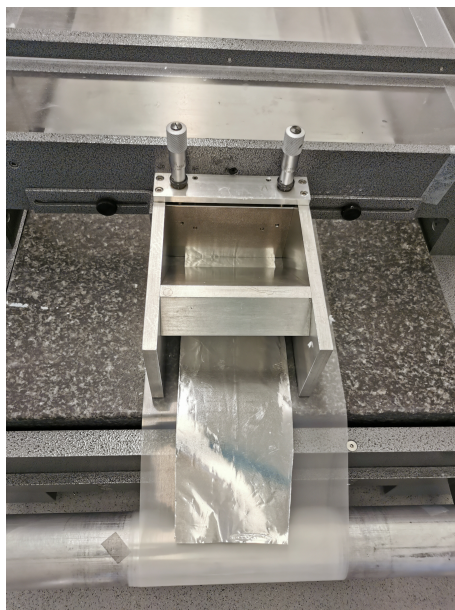
Figure 3.3: Illustration of the tape casting setup, with aluminum foil taped to the Mylar film and put into the Dr.Blade.

3.4 Particle Size Distribution

Some leftover slurry from the tape casting process was spared with the aim of performing a particle size distribution analysis. The measurements were done with a *Partica LA-960* from Horiba. This instrument measures the size distribution of a dispersion and the slurries were therefore stored in a sealed container so that the ethanol does not evaporate and the slurries become solid. The *Partica LA-960* only needs a very small amount of particles, and the slurries were therefore diluted with more ethanol to not go under 70% laser transmittance. Only a few drops of the diluted slurries were needed to obtain a laser transmittance level of 70-95%. When the distribution stabilized, three measurements were made for each prototype.

3.5 Surface Morphology

The surface morphology was studied using a *Hitachi S3400-N* scanning electron microscope with secondary electrons. The samples were cut into smaller pieces of around 1x1 cm. The accelerating voltage was set to 20kV and the working distance to 4.2mm.

3.6 Surface Wetting Properties

The wetting properties were investigated using a *Krüss Drop Shape Analyser DSA100*. Figure 3.4 shows the instrument with a *HC40* temperature chamber mounted to

reach temperatures around freezing point of water; 0°C.

A 4x4cm sample was fastened using double-sided tape. Using the *Krüss ADVANCE* software with sessile drop mode, a program was set to deposit a 8 µL droplet at a speed of 20 $\frac{\mu L}{s}$. Measurements were done every second for 15 seconds and tangent 1 was used as the ellipse fitting mode to measure the contact angle.
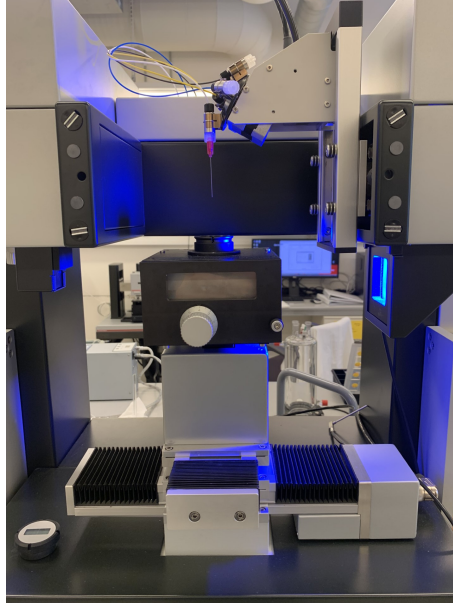

Figure 3.4: Illustration of the experimental setup for the DSA test. The temperature chamber is the black chamber in the middle of the picture. The needle with pink plastic is the syringe and where the water comes from. The syringe goes into the chamber before the droplet is deposited onto the coating. Both the chamber and the syringe are adjustable in all directions.

3.7 Mechanical Properties

The mechanical properties of the coatings were tested with a *Anton Paar Micro Scratch Test* instrument. Since the prototypes only consist of the 50 µm coating on top of 50 µm aluminum foil they are bendable and had to be taped onto a steel substrate (Steel St52) before the scratching.
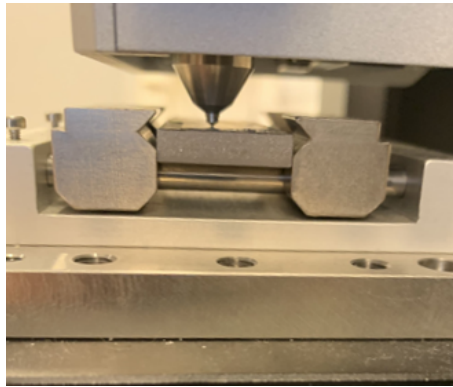
Figure 3.5: *Anton Paar Micro Scratch Test* instrument with a sample mounted. The image was taken just before the scratch test began.

The indenter used was a *Rockwell S-023* of diamond with a radius of $20\,\mu m$. The scratch was linear. The first step includes a pre-scan of the surface. This was set to $30\,mN$. For the main step the start load was set to $30\,mN$ and the end load to $300\,mN$ with a loading rate of $270\,\frac{mN}{min}$. The last step includes a post-scan to see the coating recovery. The de-loading rate was set to $6\,mN$ and the pause before post-scan was set to be $60\,s$.

Panoramic images were captured with this instrument, and additional SEM images were taken later on with different magnifications.

3.8 De-icing characterization

The de-icing characterization consists of multiple different experiments divided into two main groups; horizontal setup and vertical setup. The vertical setup measures when the droplets glide off the coatings after melting, while the horizontal setup measures the moment the droplet melts. These setups are further divided into experiments with illumination and with minimal illumination. One experiment was done outside and is further explained in the last subchapter.

The de-icing characteristics were investigated inside a styrofoam box as illustrated in Figure 3.7. All four prototypes were tested with water droplets of $20\,\mu L$ on each. A piece of commercial duct tape was used as a reference sample. The prototypes and the reference sample were taped to an aluminum plate and further placed into a freezer with -20[°]. The aluminum plate had to be horizontal in the freezer, as shown in Figure 3.6 to obtain uniform droplets.
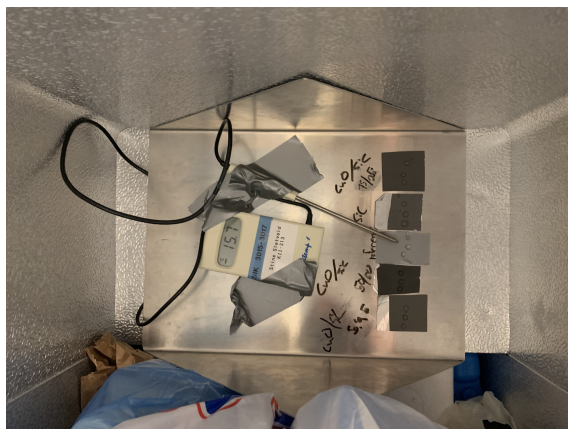
Figure 3.6: Prototypes taped to an aluminum plate placed in the freezer. They are lying horizontally.

Droplets of 20 µL were depositted on the coatings in the freezer using a *Eppendorf Research plus* 20-200 µL micro-pipette. While the droplets were in the freezer the styrofoam box was filled with around 1kg of crushed ice and six freezer elements were placed along the walls. The freezer elements needed to be spread evenly along the edges inside the styrofoam box to achieve an even temperature distribution. The styrofoam box would start with temperatures around -9.5°C and increase to 0° after 60 minutes. When all the droplets were frozen, the aluminum plate was transferred into the styrofoam box.

3.8.1   Horizontal setup

The aluminum plate was laid down horizontally along the bottom of the box. A light bulb with 1050 lm were taped to the lid, 10 cm from the prototypes. A temperature sensor was used to get an overview of the temperature distribution, as well as to measure the temperature change during the experiment. The temperature sensor was placed as close to the samples as possible. Lastly, a *GoPro Hero 11 Black* was taped to the lid, positioned directly above the prototypes, and set to take a time-lapse of the melting droplets. The time-lapse took pictures every 10 second. Once the frozen droplet changed color from white to transparent, the time was noted as the melting time.
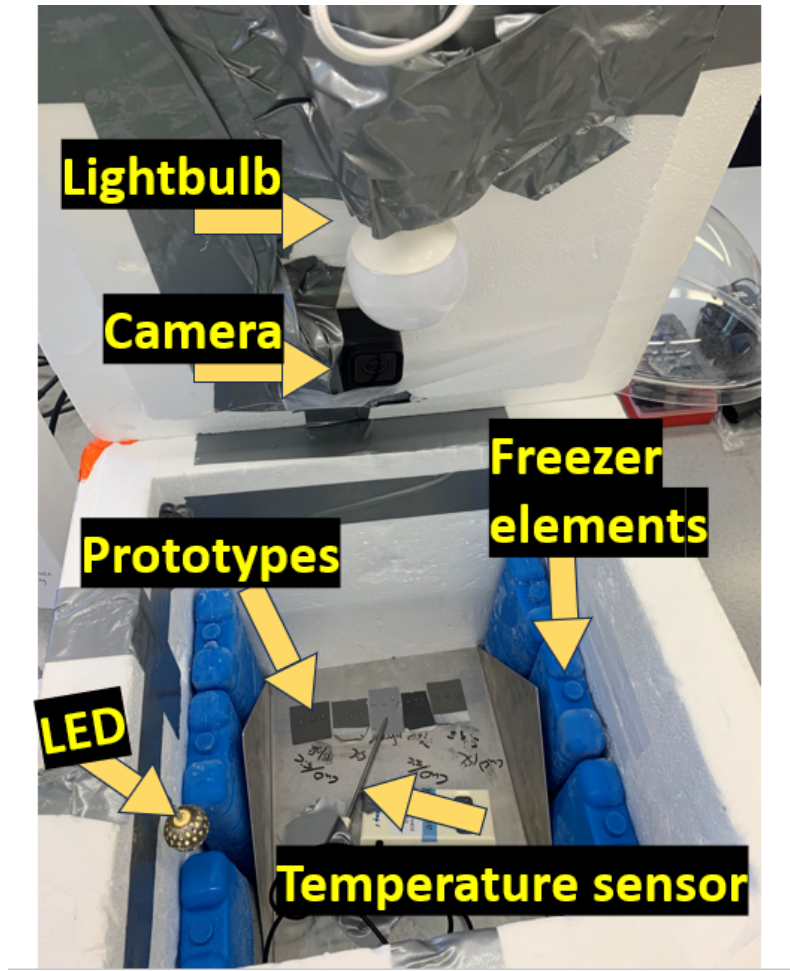
Figure 3.7: Picture of the experimental setup of the de-icing experiment with aluminum plate lying down. Six samples were tested with droplets of 20 µL each. The samples were taped to an aluminum plate that lies flat along the bottom of the styrofoam box. A 1050 lm light bulb was placed at a distance 10 cm from the prototypes, and taped to the lid of the box. Freezer elements are placed on all sides of the box, a temperature sensor is placed close to the samples, and a GoPro camera was taped to the lid to capture a time-lapse of the melting behavior of the different prototypes.

3.8.2 Vertical setup

For the vertical setup, the aluminum plate was standing up 90° vertically, as shown in Figure 3.8. This is to see when the droplets glide off the coating. The prototypes were taped as far down on the plate as possible to get the lowest temperature possible inside the styrofoam box. Both the light bulb and the GoPro camera were taped to the opposite wall of where the aluminum plate was placed, and not to the lid like in the horizontal setup. Soon after the melting began, the droplets would glide downwards, and the time was noted.

Figure 3.8: Overview of the experimental setup for de-icing characterization with the aluminum plate standing vertically.

3.8.3 Illumination vs minimal illumination

A small LED light, shown to the left in Figure 3.8, was placed inside the styrofoam box to allow just enough light for the GoPro to capture the melting time of the droplets. It gives out a small amount of light and acts as the only light source when the 1050 lm light bulb is turned off. Two experiments were carried out with the LED as the only light source, one with the vertical setup and one with the horizontal setup.

3.8.4 De-icing outside

One de-icing test was carried out outside. This test was dependent on the weather, and the test was done one morning when the temperature outside was below 0°. The start of the experiment was similar to the ones mentioned above, with the prototypes placed in the freezer and droplets deposited onto the coatings. Six samples of both the SiC prototype and the 50/50 prototype were used for this experiment. They were placed in two rows every other over. This time the styrofoam box was not filled with either crushed ice or freezer elements. The box was placed outside while the prototypes were in the freezer. Once the droplets were frozen, the box was brought in, the prototypes were placed inside the box horizontally, and the box was brought

back outside. This step needs to be as fast as possible to keep the temperature below 0°C. Once the frozen droplets changed color from white to transparent, the melting time was noted.

4 Results

4.1 Raw powder characterization

Figure 4.1 shows the agglomerates of the SiC powder before the ball milling. They appear as quite big spherical agglomerates, which is a normal structure after spray-drying ceramic powders. The SiC agglomerates are in the range of 10 µm to 250 µm. The CuO nanopowder is less clustered up and does not form spherical agglomerates. The CuO powder consists of smaller particles evenly spread on a flat surface. Some smaller clusters are visible. These are in the range of 10 µm to 100 µm.
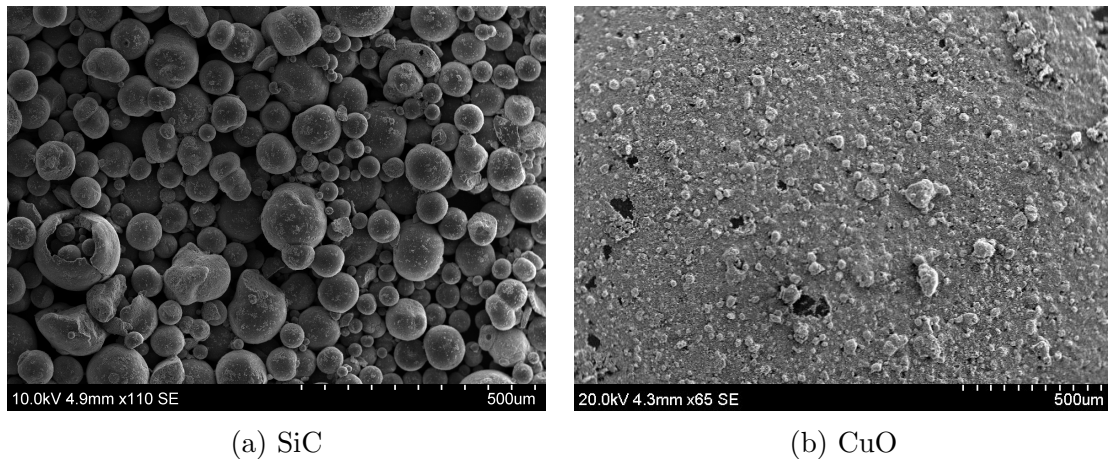

| (a) SiC | (b) CuO |

Figure 4.1: SEM images of SiC and CuO raw powder before the milling step.

4.2 Slurry characterization

Figure 4.2 shows the particle size distributions for the 4 prototype coatings. The 50/50 prototype does have the smallest particles with a mean size of 2.39 µm. The 75/25 and the 95/5 prototypes have the largest particles with a mean sizes of 15.8 µm and 5.9 µm respectively. There are however particles ranging between 20-400µm for both of these prototypes, which can be because of unbroken agglomerates. The SiC prototype does show the least amount of agglomerates, but its particle size distribution peak shows a slightly larger size than for all the prototypes containing CuO.

4.3 Coating charaterization

The SEM images in Figure 4.3 show the coating of all four prototypes. Figure 4.3a shows the coating with SiC only. This coating consists of sharp and rigid SiC particles, with most particles not larger than a few microns. A few larger particles are visible in the range of 5 µm. These larger SiC particles are also present in the latter coatings and are easy to distinguish from the CuO nanopowder. Figure 4.3b, Figure 4.3c and Figure 4.3d all show similar surfaces, with larger SiC particles mixed
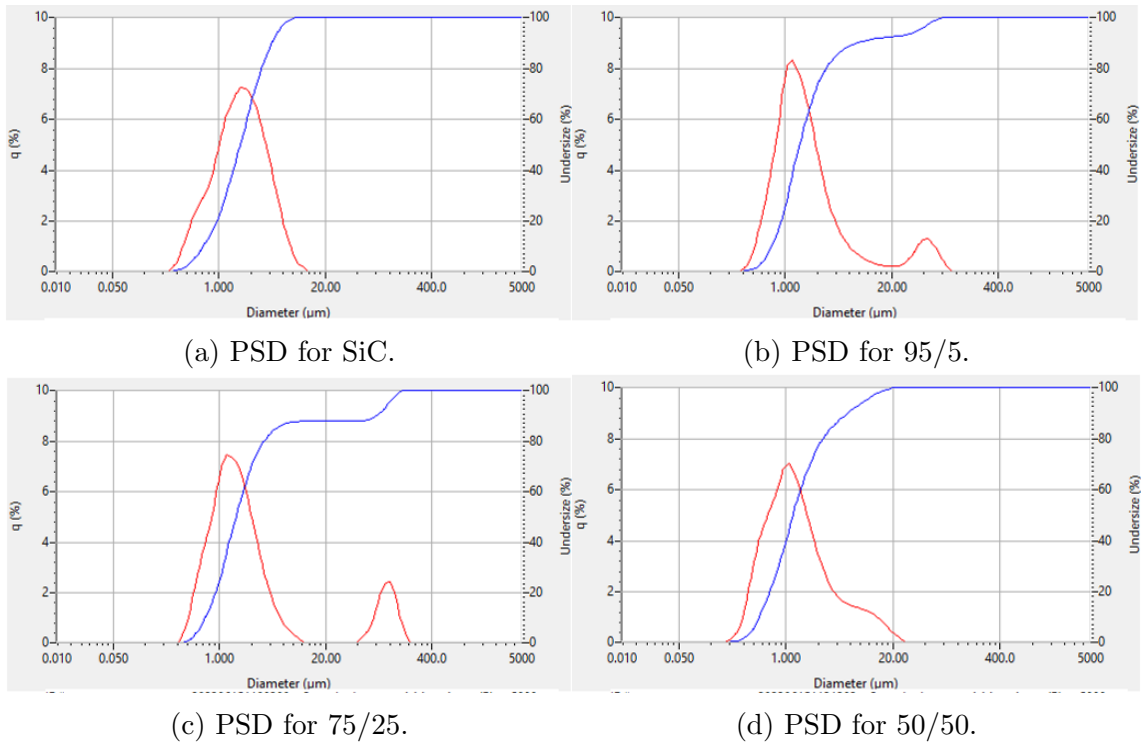
(a) PSD for SiC.

(b) PSD for 95/5.

(c) PSD for 75/25.

(d) PSD for 50/50.

Figure 4.2: Particle size distribution for the four prototypes. The x-axis shows the diameter in µm and the y-axis represents the frequency of occurrences. The red curve is the particle size distribution and the blue curve is the cumulative curve showing the undersize meaning for each size of particles which % of the sample has a size lower or equal than the value in x axis.

with smaller CuO particles. The 50/50 SiC/CuO coating does have the least amount of larger SiC particles, which is expected as it also contains the least amount of SiC. The four coatings are all evenly distributed and have few defects and little to no visible contamination.

4.4 Coating preparation

Figure 4.4 shows the SiC slurry cast onto 30cm long aluminum strips. The coating appears grey with some uneven coated parts along the edges. The coating on the right is also partly ripped. The ripped and uneven parts were not used further.
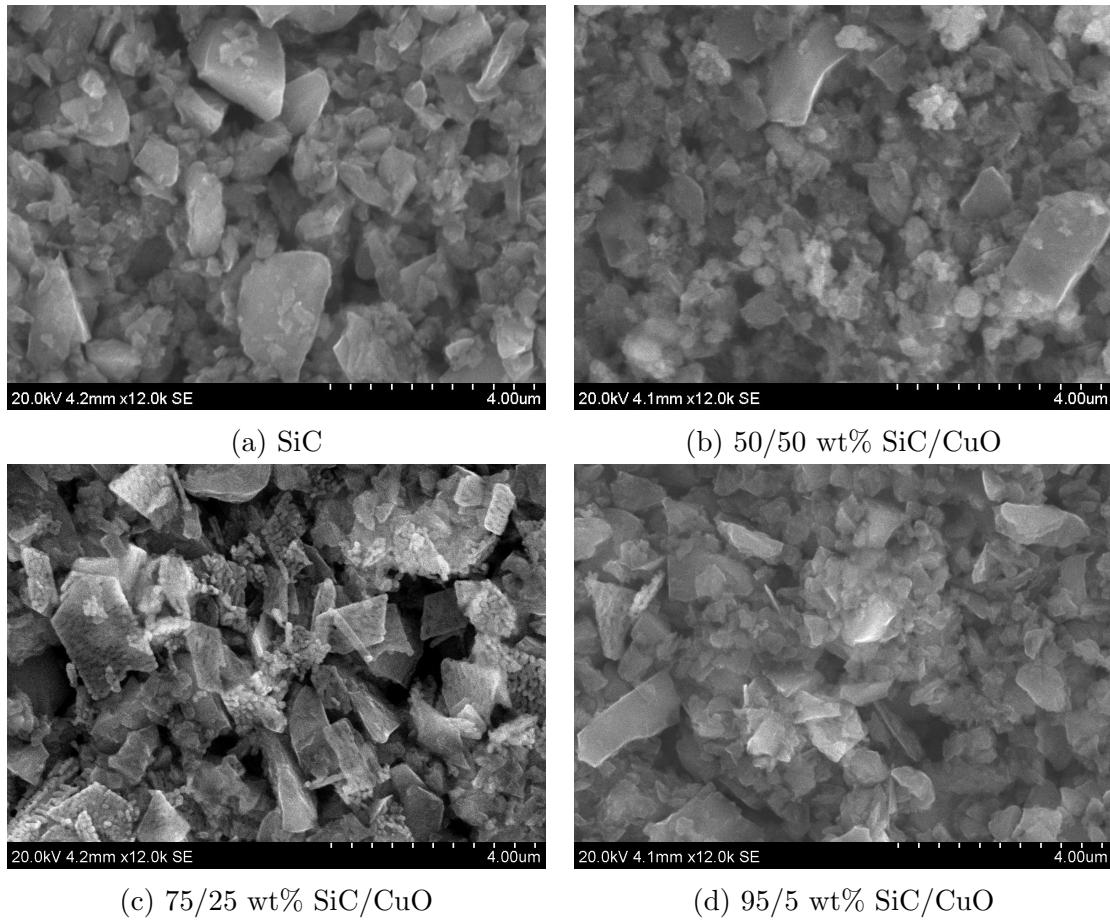
(a) SiC

(b) 50/50 wt% SiC/CuO

(c) 75/25 wt% SiC/CuO

(d) 95/5 wt% SiC/CuO

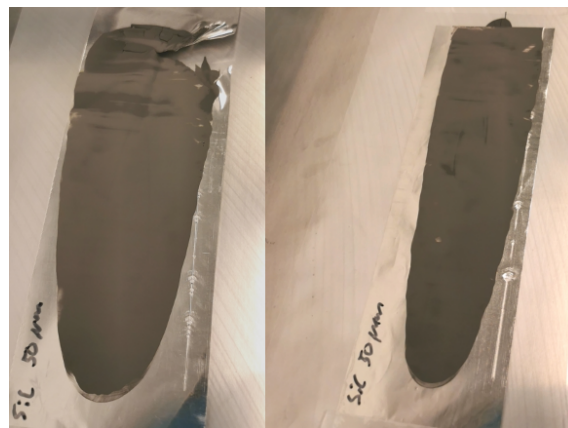Figure 4.3: SEM images of SiC and SiC/Cuo coatings

Figure 4.4: 30 cm long aluminium strips with 50 µm thick SiC coating. These two strips have the same coating, but the one to the left was damaged during the tape casting process.

One sample from each prototype is presented in Figure 4.5. The coating is evenly spread and you can see a slight color difference, where the darkest color belongs to the coating with the most CuO. The prototype samples are ordered with a decreasing

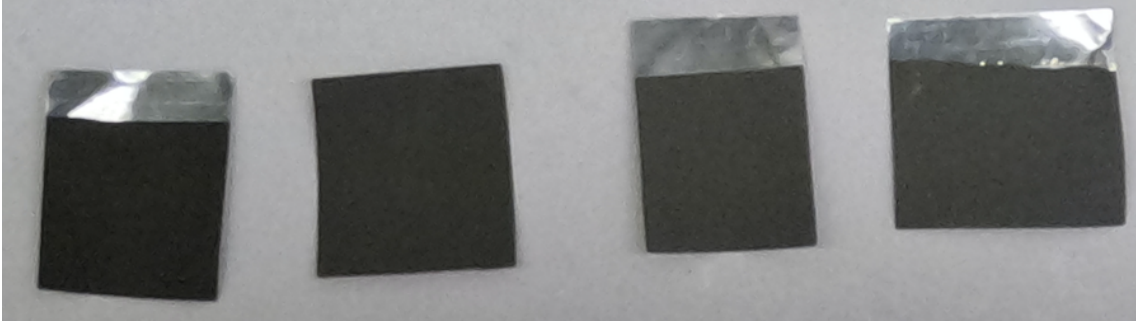amount of CuO from left to right.

Figure 4.5: 4 cm × 4 cm aluminium pieces with 50 µm thick coating. The samples are ordered with decreasing amounts of CuO from left to right: 50wt%, 25wt%, 5wt%, and 0wt%.

Table 5 shows an overview of the weight of 1x1cm of each prototype and the weight of a 1x1cm piece of aluminum with no coating as reference. The 75/25 prototype is the heaviest, while the latter three have similar densities.

Table 5: Overview of the weight of each prototype.

Prototype	Weight [g]
SiC	0.069
95/5	0.066
75/25	0.104
50/50	0.070
Aluminium	0.062

Figure 4.6 and Figure 4.7 shows SEM-images of the cross-section of the absorber layer. Figure 4.7 shows two images with different magnifications of the SiC prototype. Figure 4.6 shows two images with different magnification of the 75/25 SiC/CuO prototypes. The cross-section of the absorber layer is 50 µm along the entire edge for both the SiC and the 75/25 SiC/CuO prototypes.
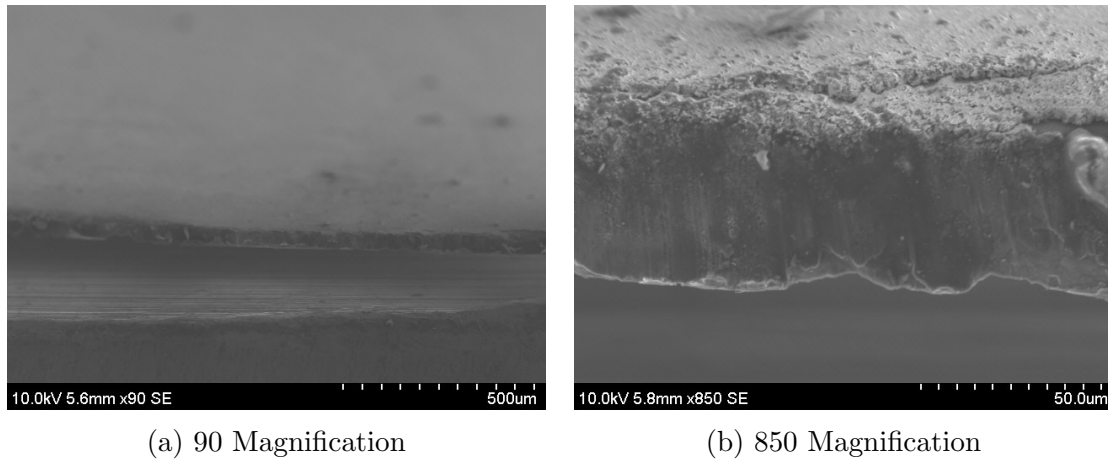
(a) 90 Magnification   (b) 850 Magnification

Figure 4.6: Cross-section of absorber layer of 75/25 SiC/CuO prototype with (a) low magnification and (b) high magnification.

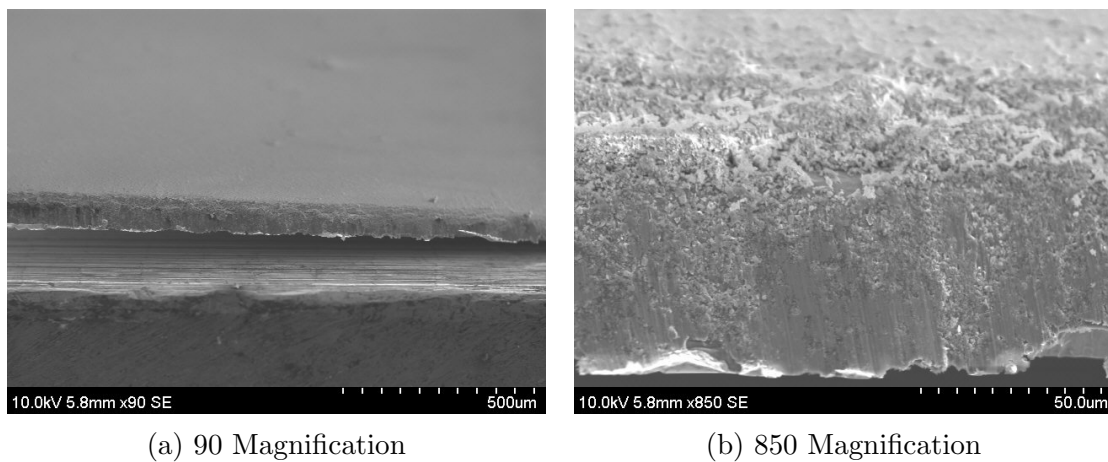(a) 90 Magnification   (b) 850 Magnification

Figure 4.7: Cross-section of absorber layer of SiC the prototype with (a) low magnification and (b) high magnification.

4.5 Wetting properties

Figure 4.8 and Figure 4.8 shows images of two of the droplets used in the characterization. Both images are taken 15 seconds after the deposition.

Table 6 shows an overview of the results from the water contact angle measurements. The 75/25 prototype is the only prototype with a coating showing hydrophobic properties, with a water contact angle larger than 90°. The remaining three prototypes have hydrophilic coatings. The 50/50 prototype has a larger angle than the SiC- and the 95/5 prototype, while the two latter coatings show similar wetting properties with angles of 52.7° and 49.8° respectively.

Figure 4.8: Image taken with a 3.8 µL droplet and its water contact angle to the SiC prototype coating. The water contact angle is 52.7°.
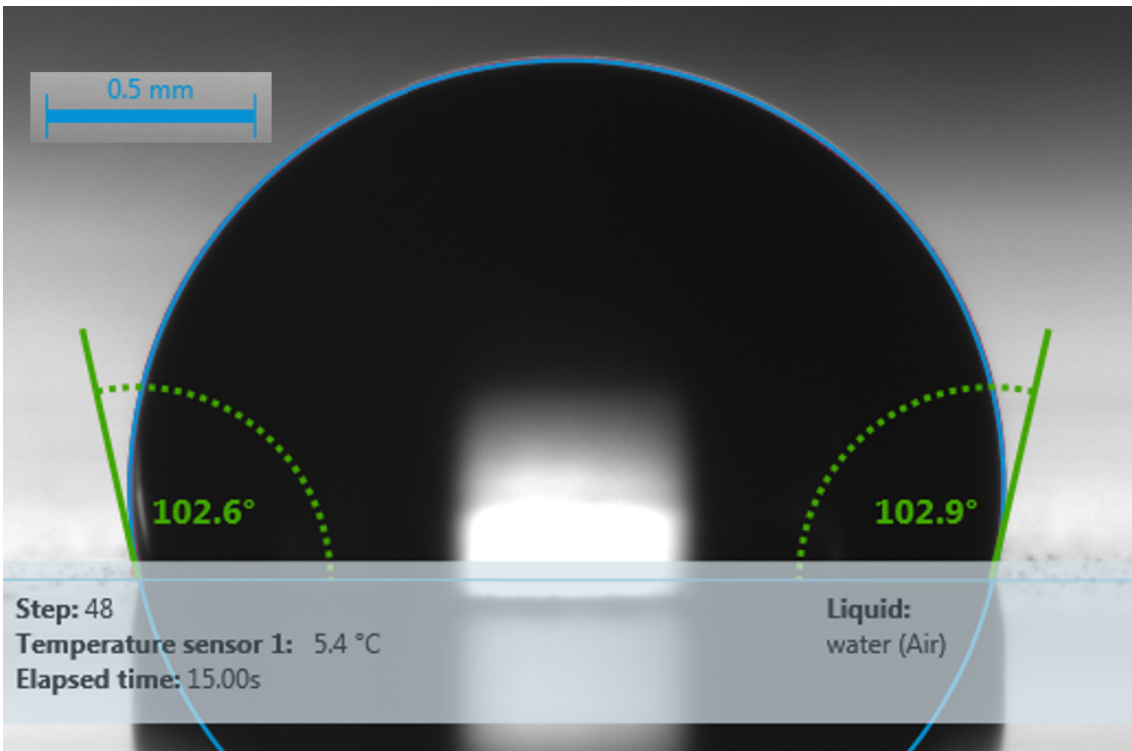

Figure 4.9: Image taken with a 3.0 µL droplet and its water contact angle to the 75/25 prototype coating. The water contact angle is 102.8°

Table 6: Overview of WCA, drop size, and temperature during measurements.

Prototype	Water contact angle[°]	Drop size [μL]	Temperature[°C]
SiC	52.7	3.8	2.9
95/5	49.8	2.2	3.8
75/25	102.8	3.0	5.4
50/50	77.4	4.3	4.5

4.6 Durability

The durability section consists of results from a micro scratch test where the penetration depth vs residual depth was investigated. The scratch was visualized with a panoramic image and characterized with images using SEM. The entire scratch is 3mm long and did not fit into one SEM image alone, and the SEM image of the entire scratch therefore consists of two images put together, shown in Figure 4.10, Figure 4.14, Figure 4.18 and Figure 4.22. The results from each prototype are presented separately in the results section and further explained and compared to each other in the discussion section.

4.6.1 Durability for SiC prototype

Figure 4.10 shows two SEM images put together to show the entire scratch on the SiC prototype. Figure 4.11 shows the start and the end of the scratch. Figure 4.12 shows a panoramic image of the entire scratch using an optical microscope. Figure 4.13 shows the penetration depth plotted vs the residual depth.
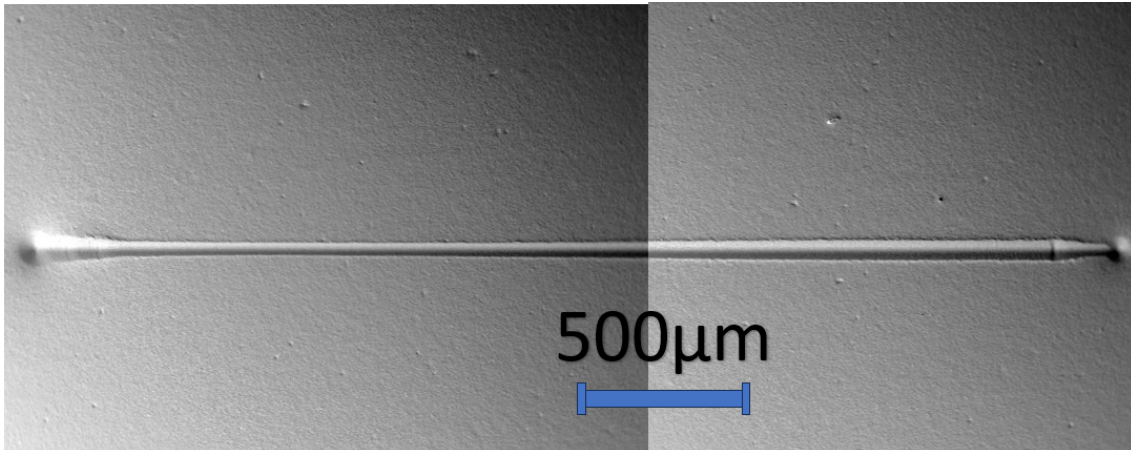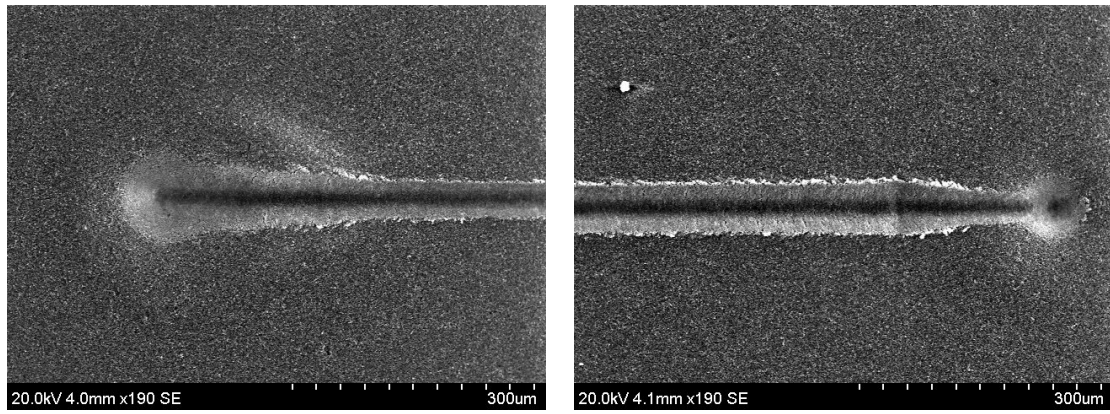

Figure 4.10: SEM-image of the entire scratch on the SiC prototype. Backscattered electrons were used for imaging. This image consists of two images put together to show the whole scratch. The scratch starts from the left and ends on the right.

(a) The start of the scratch on the SiC prototype.

(b) The end of the scratch on the SiC prototype.

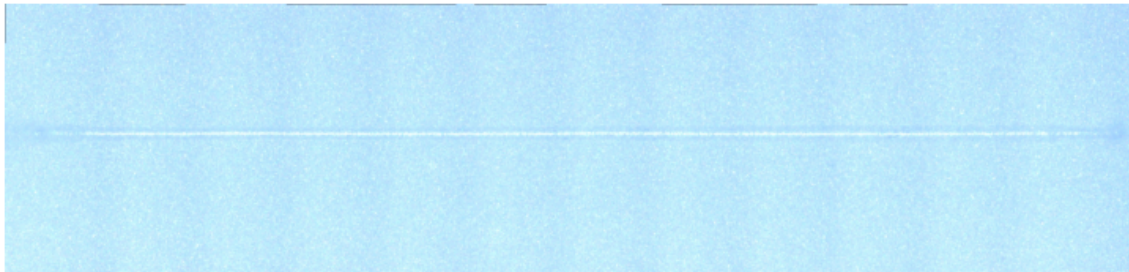Figure 4.11: SEM images of the start and end of the scratch on the SiC prototype.

Figure 4.12: Panoramic image of the entire 3 mm scratch of the SiC prototype using an optical microscope mounted to the *Anton Paar Micro Scratch Test* instrument.
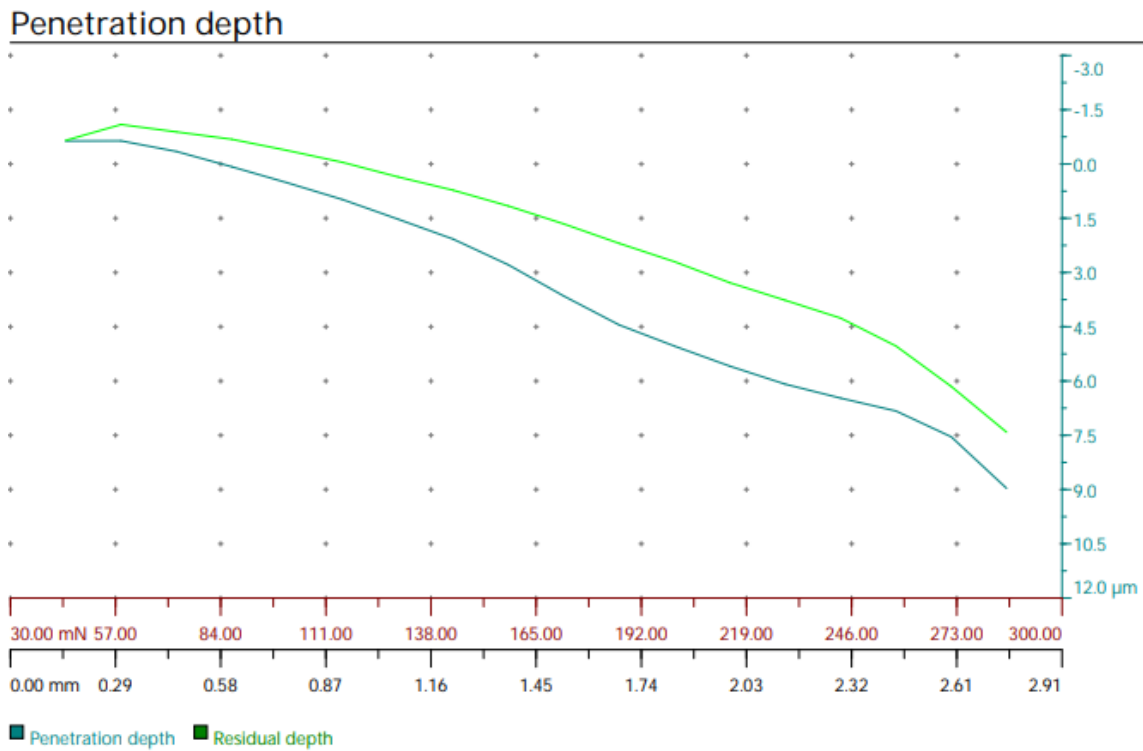
Figure 4.13: Penetration depth vs residual depth on the SiC scratch. The X-axis shows both the applied load measured in µm (red), and the distance moved measured in mm (black). The Y-axis shows the coating depth measured in µm.

4.6.2 Durability for 50/50 prototype

Figure 4.14 shows two SEM images put together to show the entire scratch on the 50/50 prototype. Figure 4.15 shows the start and the end of the scratch. Figure 4.16 shows a panoramic image of the entire scratch using an optical microscope. Figure 4.17 shows the penetration depth plotted vs the residual depth.
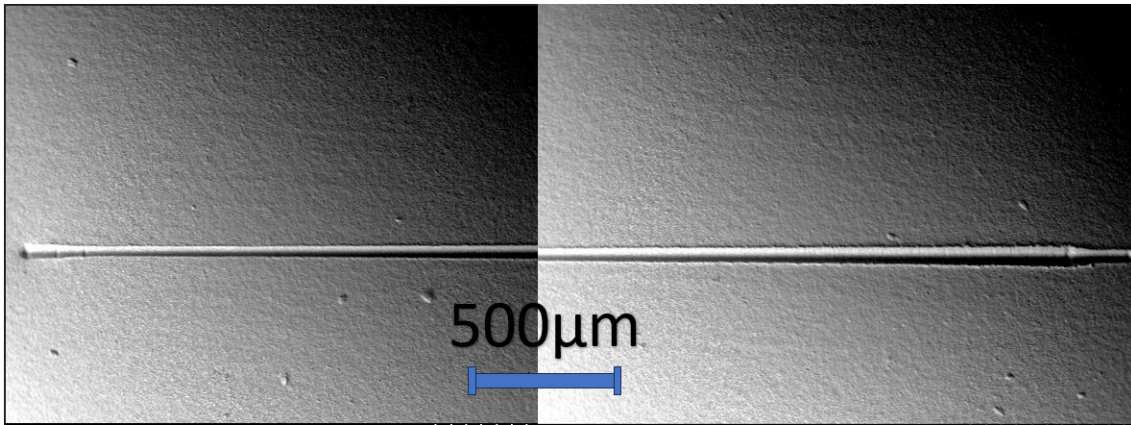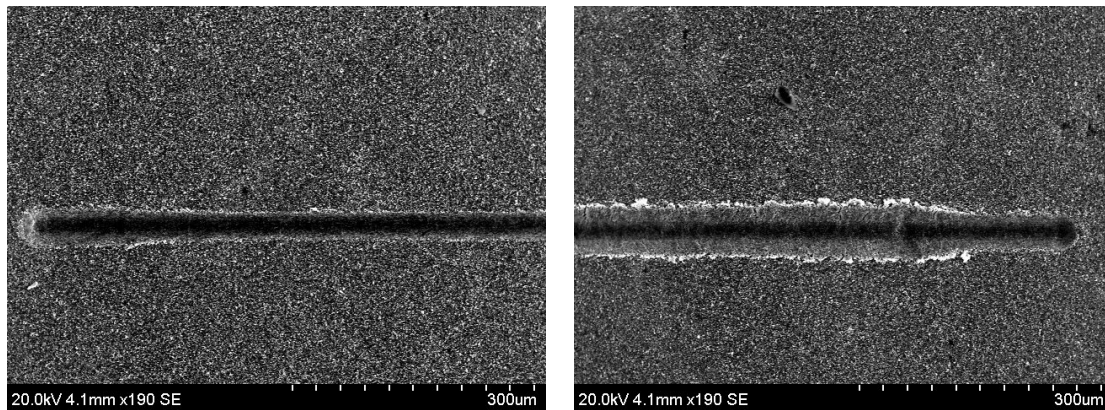
Figure 4.14: SEM-image of the entire scratch on the 50/50 SiC/CuO prototype. Backscattered electrons were used for imaging. This image consists of two images put together to show the whole scratch. The scratch starts from the left and ends on the right.

(a) The start of the scratch on the 50/50 pro-
totype.

(b) The end of the scratch on the 50/50 pro-
totype.

Figure 4.15: SEM images of the start and end of the scratch on the 50/50 SiC/CuO prototype.

Figure 4.16: Panoramic image of the entire 3 mm scratch of the 50/50 SiC/CuO prototype using an optical microscope mounted to the *Anton Paar Micro Scratch Test* instrument. The focus was off and the scratch is therefore not easy to see.

Figure 4.17: Penetration depth vs residual depth on the 50/50 CuO/SiC scratch. The X-axis shows both the applied load in µm (red) and the distance moved in mm (black). The Y-axis shows the coating depth in µm.

4.6.3 Durability for 75/25 prototype

Figure 4.18 shows two SEM images put together to show the entire scratch on the 75/25 prototype. Figure 4.19 shows the start and the end of the scratch. Figure 4.20 shows a panoramic image of the entire scratch using an optical microscope. Figure 4.21 shows the penetration depth plotted vs the residual depth.

Figure 4.18: SEM-image of the entire scratch on the 75/25 prototype. Secondary electrons were used for imaging. This image consists of two images put together to show the whole scratch. The scratch starts from the right and ends on the left.

(a) The start of the scratch on the 75/25 prototype.

(b) The end of the scratch on the 75/25 prototype.

Figure 4.19: SEM images of the start and end of the scratch on the 75/25 SiC/CuO prototype.

Figure 4.20: Panoramic image of the entire 3 mm scratch of the 75/25 SiC/CuO prototype using an optical microscope mounted to the *Anton Paar Micro Scratch Test* instrument.
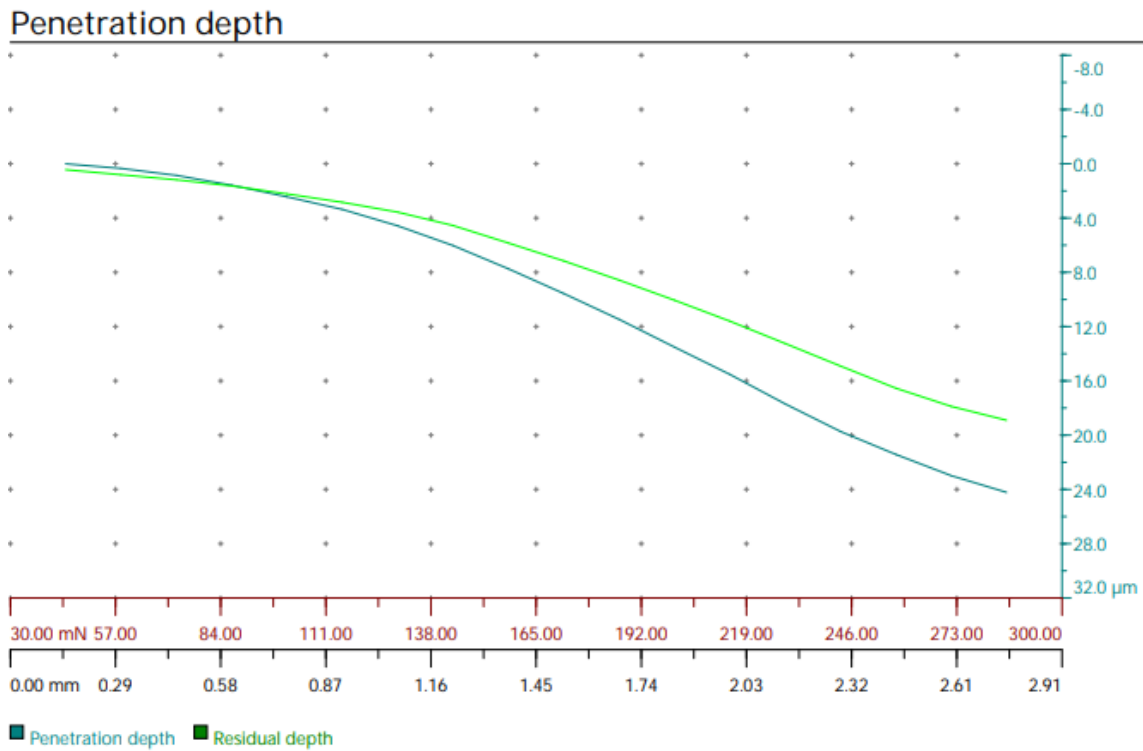
Penetration depth

Figure 4.21: Penetration depth vs residual depth on the 75/25 CuO/SiC scratch. The X-axis shows both the applied load in µm (red), and the distance moved in mm (black). The Y-axis shows the coating depth in µm.

4.6.4 Durability for 95/5 prototype

Figure 4.22 shows two SEM images put together to show the entire scratch on the 95/5 prototype. Figure 4.23 shows the start and the end of the scratch. Figure 4.24 shows a panoramic image of the entire scratch using an optical microscope. Figure 4.25 shows the penetration depth plotted vs the residual depth.
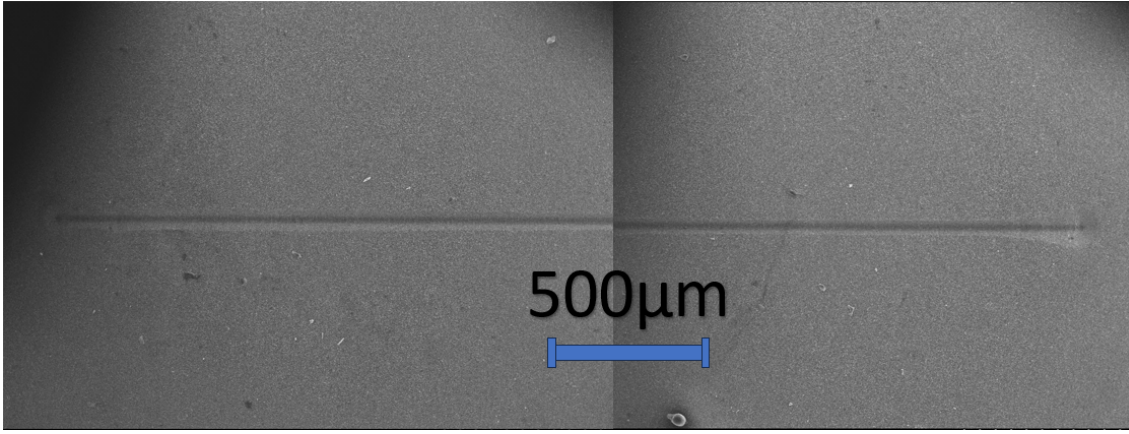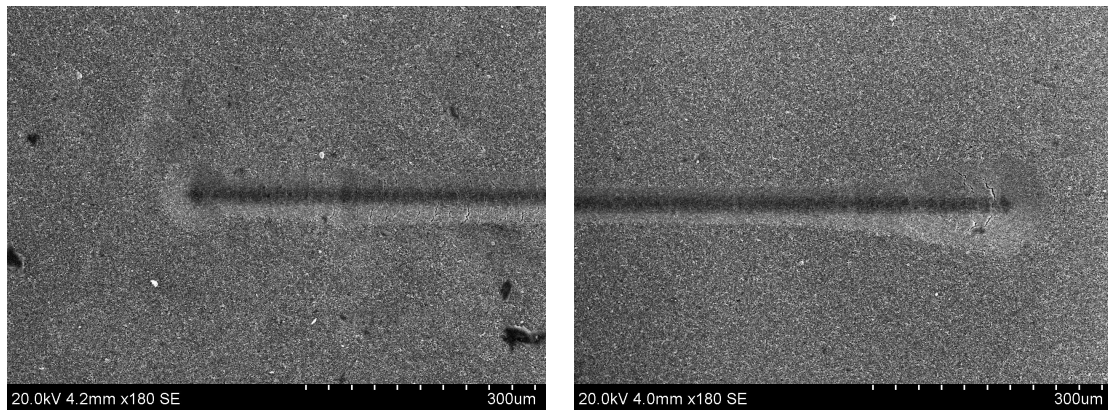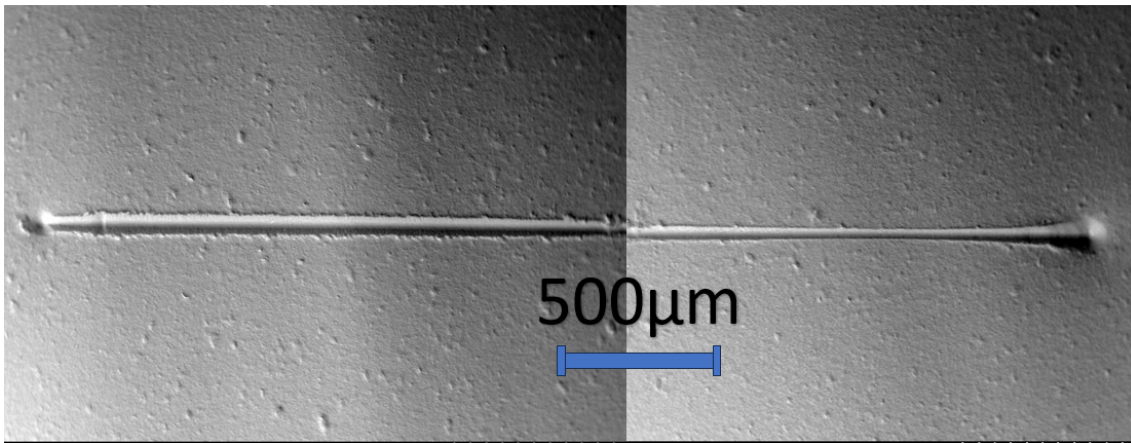
Figure 4.22: SEM-image of the entire scratch on the 95/5 prototype. Backscattered electrons were used for imaging. This image consists of two images put together to show the whole scratch. The scratch starts from the right and ends on the left.
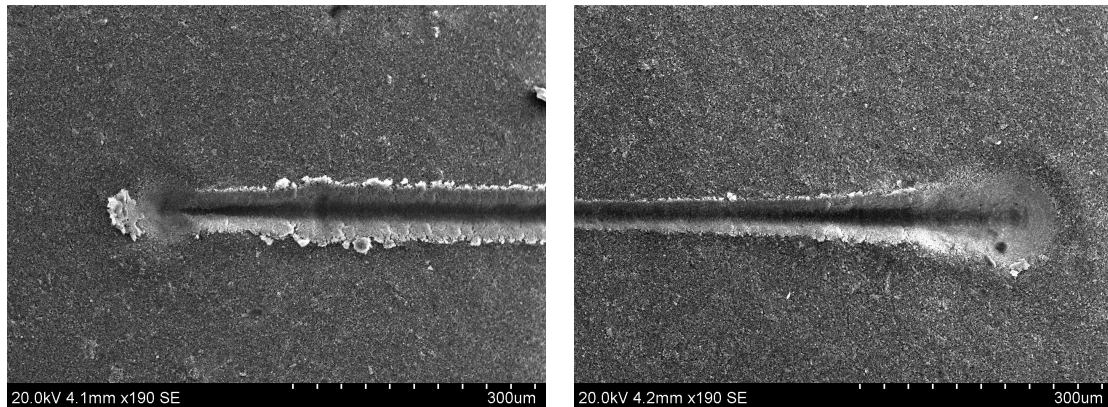
(a) The end of the scratch on the SiC proto-type.

(b) The start of the scratch on the SiC pro-totype.

Figure 4.23: SEM images of the start and end of the scratch on the 95/5 SiC/CuO prototype.
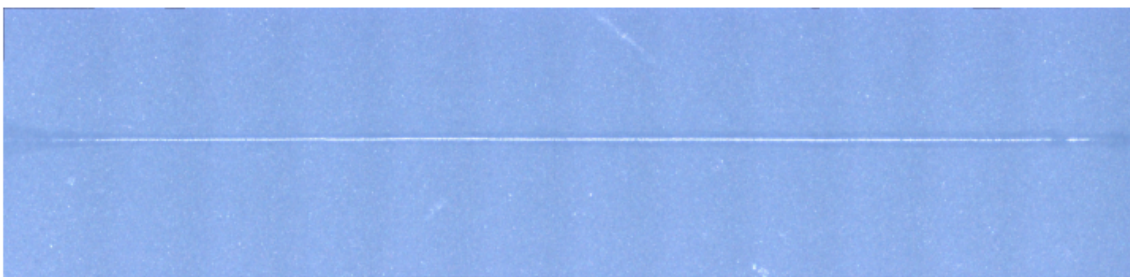
Figure 4.24: Panoramic image of the entire 3 mm scratch of the 95/5 SiC/CuO prototype using an optical microscope mounted to the *Anton Paar Micro Scratch Test* instrument.
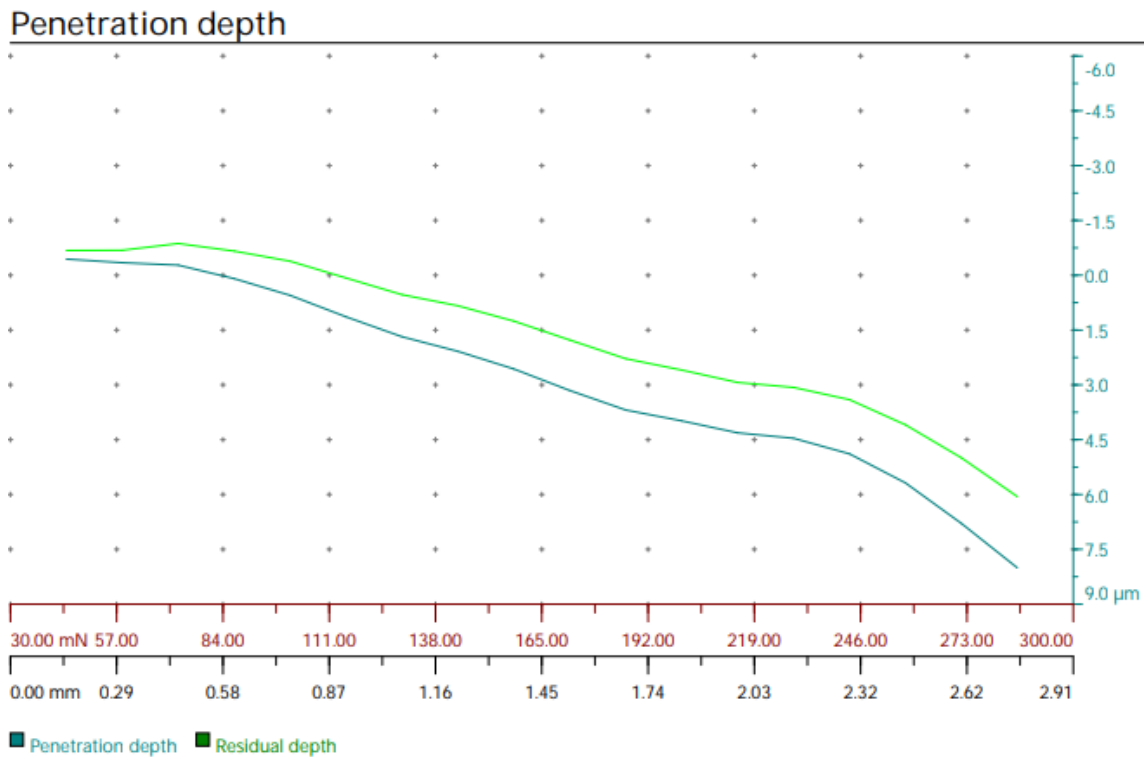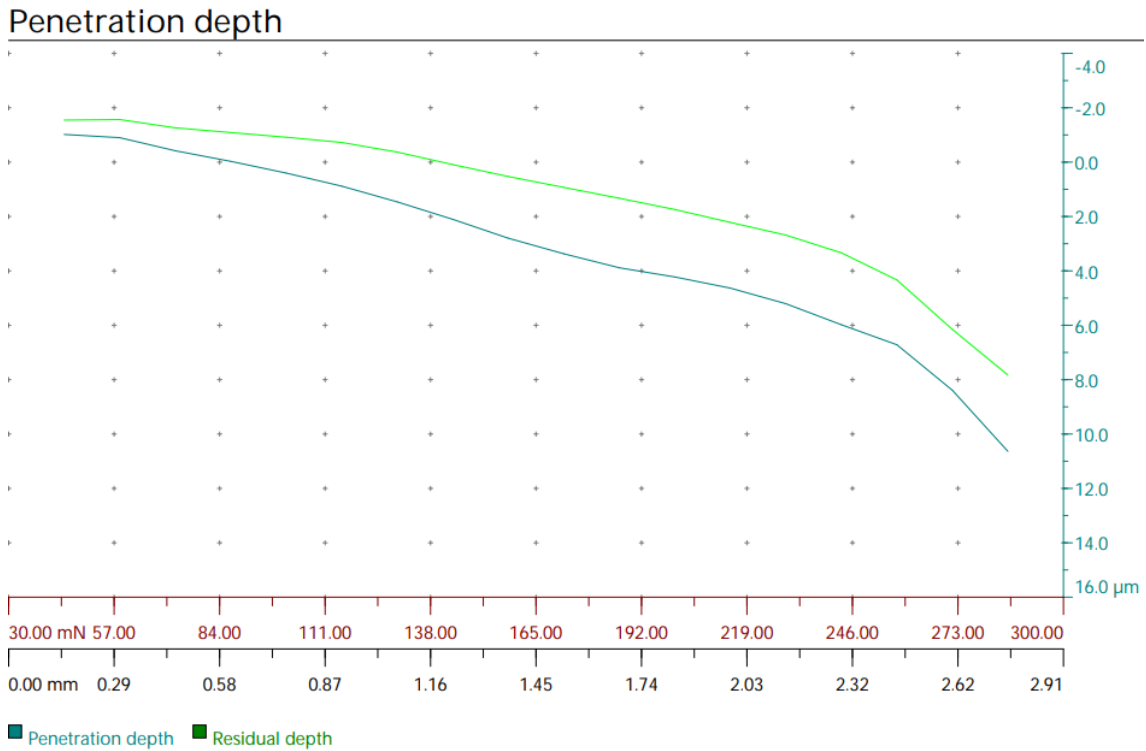
Figure 4.25: Penetration depth vs residual depth on the 95/5 CuO/SiC scratch. The X-axis shows both the applied load in µm (red), and the distance moved in mm (black). The Y-axis shows the coating depth in µm.

4.7 De-Icing

The results from the de-icing experiments with horizontal and vertical setups are presented separately. The experiments with illumination and with minimal illumination are presented under both the horizontal and the vertical setup. The experiment carried out outside is presented at the end.

4.7.1 Horizontal setup

Figure 4.26 shows two images of the prototypes in the horizontal setup with illumination. Figure 4.26a shows the prototypes with frozen droplets, and Figure 4.26b shows the same setup after some of the droplets had melted. The SiC located second to the right shows a clear difference from (a) to (b). This was also the coating that had the fastest melting time among the coatings for this setup.

Figure 4.27 shows two images of the prototypes in the horizontal setup with minimal illumination. Figure 4.27a shows the prototypes with frozen droplets, and Figure 4.27b shows the same setup after some of the droplets had melted.

Table 7 shows an overview of the prototypes and reference sample, and their melting

(a) Frozen droplets.   (b) Melting droplets.

Figure 4.26: The four prototypes plus one reference sample, with frozen droplets in (a) and with melting droplets in (b). The ordering in both images are from left to right; 95/5, 50/50, reference sample, SiC, and 75/25.

(a) Frozen droplets.   (b) Melted droplets.

Figure 4.27: The four prototypes plus one reference sample, with frozen droplets in (a) and with melting droplets in (b). The ordering in both images are from left to right; 95/5, 50/50, reference sample, SiC, and 75/25.

time. The SiC and 75/25 prototypes proved to be melting the fastest with 210s and 220s respectively. All prototypes had a faster melting time than the reference sample with a 790s melting time.

Table 7: Overview of the melting time of the prototypes and the reference sample, both with illumination and with minimal illumination.

Prototype	Melting time with illumination [s]	Melting time with minimal illumination [s]
SiC	210	450
95/5	290	590
75/25	220	480
50/50	350	710
Reference	790	1200

4.7.2   Vertical setup

Figure 4.28 shows two images of the prototypes in the vertical setup with illumination. Figure 4.28a shows the prototypes with frozen droplets, and Figure 4.28b shows the same setup after some of the droplets had melted. SiC had the quickest time before the droplet slides, with 260s. The 50/50 prototype used 400s and the reference sample used 800s.

(a) Frozen droplets.   (b) Melted droplets starting to slide down.
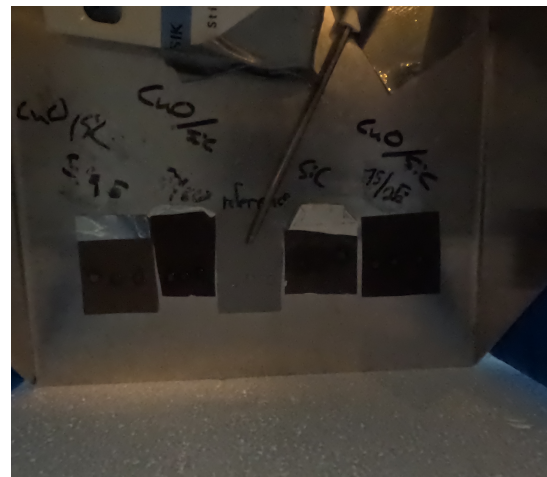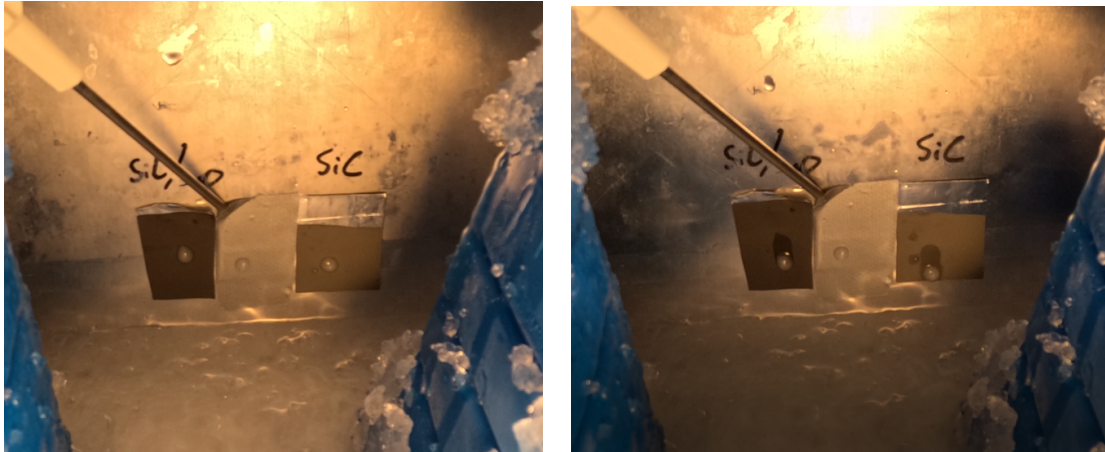
Figure 4.28: Two prototypes plus one reference sample, with frozen droplets in (a) and with melting droplets in (b). The ordering in both images are from left to right; 50/50, reference sample, SiC.

Figure 4.29 shows two images of the prototypes in the vertical setup with minimal illumination. Figure 4.29a shows the prototypes with frozen droplets, and Figure 4.29b shows the same setup after some of the droplets had melted. SiC had the quickest time before the droplet slides, with 550s. The 50/50 prototype used 800s and the reference sample used 900s.

Table 8 shows the results from the vertical setup. The time refers to when the droplets started sliding down. The SiC prototype had the fastest time both for the experiment with illumination and with minimal illumination; 260s and 550s respectively. The reference sample was again the slowest, using double the time of the 50/50

(a) Frozen droplets.

(b) Melted droplets.

Figure 4.29: Two prototypes plus one reference sample, with frozen droplets in (a) and with melting droplets in (b). The ordering in both images are from left to right; 50/50, reference sample, SiC.

prototype. The time also doubled for both the SiC and the 50/50 prototype when using minimal illumination, while just increasing 11% for the reference sample.

Table 8: Overview of the time before the droplets slide downwards for SiC, 50/50, and a reference sample.

Prototype	Melting time with illumination [s]	Melting time with minimal illumination [s]
SiC	260	550
50/50	400	800
Ref.	800	900

4.7.3 Outside setup

Figure 4.30 shows two images from the experiment done outside. This experiment showed close to equal melting time for the two prototypes tested, namely the SiC and 50/50.

Table 9 shows an overview of the melting time for the two prototypes tested outside.

Table 9: Overview of the melting time for SiC and 50/50 prototypes.

Prototype	Melting time with illumination [s]
SiC	120
50/50	120

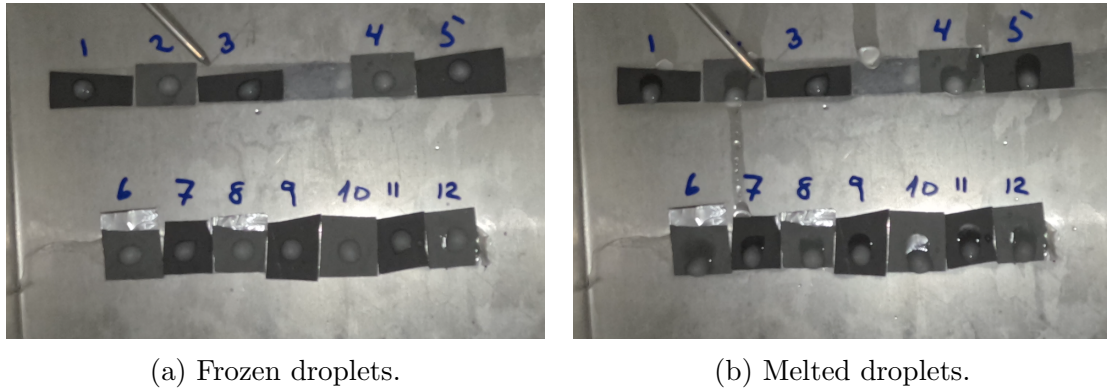(a) Frozen droplets.   (b) Melted droplets.

Figure 4.30: Six samples of the SiC and the 50/50 prototype, with frozen droplets in (a) and with melting droplets in (b). The grey coating belongs to the SiC prototype and the darker coloured coating belongs to the 50/50 prototype.

5   Discussion

This master's thesis aimed to fabricate four prototype coatings with de-icing properties, resembling the two top layers in a photothermal trap. The first section will focus on the preparation method of the coatings and will review results related to the raw powder, slurries, coatings wetting properties, and the durability of the coatings. The second section will review the de-icing properties of the four prototypes and the method of characterization.

5.1   Preparation method

5.1.1   Tape casting

The coatings were cast onto aluminum strips using a tape caster. This method is a well-established casting technique [29] which is known for its cheap, and easy-to-use, properties[30]. Normally the ceramic slurry is cast directly onto the Mylar film, but for this work, the slurry was cast onto a piece of aluminum taped to the Mylar film. This was to create the two top layers in a photothermal trap. Taping a piece of aluminum onto the Mylar film did however make the process more demanding. When the 30 x 8 cm aluminum strips had imperfections along the edges, the whole sample would be ripped and destroyed under the doctor's blade. Using aluminum foil with a thickness of 50 μm, rather than the commercial 25 μm, proved helpful. The preparation of the aluminum strips, using a ruler along the edges, would also prove to be a necessary step in the preparation before casting. Finally, about five aluminum strips were prepared for each prototype, so that any samples that were destroyed or damaged could be replaced. Figure 4.6 and Figure 4.7 show SEM-images of the cross-section of the absorber layer for the 75/25 and SiC coatings respectively. The images show that the thickness of this layer remains at about 50 μm thick along the entire surface of the samples, proving the tape casting technique successful.

Earlier studies [8] [7], using the same setup with aluminum foil taped to the Mylar

film, experienced larger variations in coating thickness. With 50 μm as targeted thickness, some of their coatings were just 4 μm thick while others were 110 μm, while also having variations of thickness along the surface. This might be a result of using different pre-measured pins. In 2022[8], a 100 μm pin was used to set the height of both the aluminum foil and the coating, while in this thesis a 50 μm pin was used on top of the 50 μm aluminum foil that was already taped to the tape caster. The pin was then dragged along the surface to make sure the height of the gap stayed 50 μm across the entire gap.

5.1.2 Wetting characteristics

The 75/25 prototype would prove the most interesting, being the only coating with hydrophobic properties. Although hydrophobic properties do not directly improve de-icing time, it is often favored because of the potential positive effects linked to self-cleaning properties[11]. The water contact angle measured for the 75/25 prototype was 102.8°. The second highest angle was for the 50/50 prototype, with 77.4°, while the SiC and 95/5 prototypes had similar hydrophilic properties with angles at around 50°. The hydrophobic properties of the 75/25 prototype can be linked to a lower degree of open porosity that was filled with water from the deposited droplet by capillary rise.

The wetting properties are often characterized when working with de-icing and anti-icing coatings, and a drop-shape analyzer was used to determine the wetting properties of the four prototypes. The instrument used, namely the *Krüss Drop Shape Analyser DSA100*, used a cold chamber that could be mounted on. The cold chamber was supposed to be screwed onto the instrument, however, the condition of the screws was poor and the chamber would not be fastened properly, leaving the chamber to vibrate slightly during the testing. This was tried countered by using a small rope tied around the chamber and trying to physically fasten the chamber this way. This reduced the vibrations slightly, and the drop shape analysis could start.

5.1.3 Durability

Four scratch tests were conducted to investigate the coating durability of the prototypes. De-icing coatings are often exposed to harsh conditions, and a robust material is needed in the absorber layer.

The amount of solvent and binder content was not changed when making the different prototypes. Earlier studies have tried varying the wt% of the binder content, to make more flexible prototypes[7]. Researchers are normally using binder contents of up to 50%. Using more binder would indeed make more flexible ceramic coatings, however increasing the binder content to values like 50% would have a significant impact on the coating's properties and would not be of interest when no thermal decomposition takes place afterward. This is further supported when the four prototypes were sufficiently flexible when bent and would not be damaged during handling.

The scratch test revealed some interesting findings, where the 75/25 prototype had the smallest penetration depth and the indenter seemed to not ever penetrate the coating, suggesting a durable material. Figure 4.18 shows the entire scratch, and compared to the other four prototypes, no penetration/damage caused by the scratch can be seen, and thus no critical value can be set. Figure 4.19a shows the end of the scratch for the 75/25 prototype, and for the other three prototypes, the images of the end of the scratch always reveal ceramic matter from the scratch on either side of the scratch. The penetration depth after 300 mN for the 75/25 prototype was 7.5 µm.

The second smallest penetration depth was for the SiC prototype, with 9.0 µm, followed by 95/5 and 50/50 with 11.4 µm and 24.0 µm respectively. All prototypes had similar residual depth, with the SiC standing out a little, with a growing difference between penetration depth and residual depth from 30 mN to 200 mN, and then the difference decreased from 200 mN to 275 mN. This tendency can be seen for the 95/5 prototype too, but not to the same extent. These two, the SiC and the 95/5, prototype are expected to show similar properties when only 5 mol% CuO is what separates them. The critical load is at about 140 mN for the SiC, 90 mN for 50/50, and 165 mN for the 95/5 prototype.

5.2 De-icing characteristics

The main focus of this Master's thesis was to make de-icing coatings. The de-icing nature of each of the prototypes was established through multiple different experimental setups. The different setups are chosen with inspiration from work performed with the same equipment from the past three years [7][8]. Some of the setups are improved, and some of the setups, like the one performed outside, are new methods of de-icing characterization. The de-icing characterization was the most time-consuming part of this thesis, when only one experiment could be done each day, because of the time the freezer elements needed to cool down. The first experiments conducted are not presented in the result section for this thesis but were rather done to map the temperature distribution throughout the chamber and to get a better understanding of how to do the de-icing experiments in a tidy way. Figure .3 is one of these experiments and shows Some of the droplets have melted along the sides, while the droplets in the middle are still frozen. Since SiC coatings are placed both on the sides as well as in the middle, and only the droplets at the sides have melted, it was thought that the temperature was higher in the middle, because of the closer distance to the light bulb. This in turn led to an increased focus on keeping the temperature low and even throughout the remaining experiments.

The styrofoam box was filled with six freezer elements and 1 kg of crushed ice before a test was conducted. The addition of ice was a new addition to the setup compared to the 2020 and 2022 setups[7][8]. An increased focus on the placement of the freezer elements, which were placed standing vertically along the walls of the styrofoam box, was also different from last year's. A final step of moving the prototypes as far down as possible on the aluminum plate to have the coating placed in the coldest parts of the box was also a contribution that made the de-icing experiments more reliable.

When making sure all the conditions mentioned above were in place, the styrofoam box would start with temperatures at around -9.5°C and increase to 0° after 60 minutes. This was enough time to measure the de-icing effect using illumination only.

Earlier studies have focused on vertical setups, to easier measure the time when the droplets slide off. With inspiration from these studies, the first experiments with vertical setups were done with the aluminum plate standing 45°. This was however increased to 90° because some of the droplets would not glide down at all with lower tilting. The fortunate result of measuring with the aluminum plate standing vertically is the easy way of seeing when the droplets melt since they would slide off shortly after melting. The problematic part about this method is that you do not only measure the de-icing time but also the hydrophobic properties of your coating. The horizontal setup was an important addition to this thesis and was conducted to measure the actual de-icing time, rather than measuring the time of sliding for the vertical setup.

The final outside setup was done to keep the temperature stable under 0°C. This was however done too late in the spring so that during the experiment the temperature outside went from -1°C to +2°C and all the droplets seemed to melt because of the temperature increasing to above 0°C.

The results from the de-icing experiments showed the best results for the SiC and the 75/25 prototype. The test with the vertical setup was only done for the SiC and 50/50 prototypes. Since the 75/25 prototype showed promising de-icing properties in the horizontal setup, and hydrophobic properties in the wetting characterization, it would be interesting to see how it would perform in the vertical setup.

6   Conclusion

In this Master's thesis, four different prototype coatings were fabricated and characterised for their de-icing properties in a photothermal trap. The coating consists of an absorbent layer and a thermal spreader layer. The thermal spreader layer consists of 50 μm thick aluminium foil and the absorber layer was prepared by casting four different ceramic slurries onto the aluminium foil with tape casting. One prototype consisted of SiC as the only ceramic powder, while three prototypes consisted of varying contents of SiC and CuO ceramic powder. The final prototypes had an absorbent layer thickness of 50 μm, making the whole prototype 100 μm thick.

The durability of the coatings was tested with a micro scratch test. This revealed similar properties for all the prototypes, except the 75/25 SiC/CuO prototype, which proved to be more durable than the rest. The 75/25 prototype was also the only prototype with a hydrophobic surface, which can be favourable for a de-icing surface because of the potential self-cleaning effect.

The de-icing characterisation revealed a successful fabrication of de-icing coatings. All prototypes would prove to have a de-icing nature, where droplets of ice would melt at below -0°C using illumination only. The shortest and best de-icing time belongs to the prototypes consisting of SiC only, and 75/25 SiC/CuO. These prototypes would only need 1/4 of the time that the reference sample needed to melt the droplets using illumination only. They also showed promising results with low illumination. The 75/25 SiC/CuO prototype is the prototype with the best results from the durability characterization, the wetting characterization and the de-icing characterization, and proved to be a durable coating that would fit the use of an absorbing layer in a photothermal trap.

7 Further work

The promising results in durability, wetting, and de-icing for the 75/25 SiC/CuO prototype suggest it to be a good fit for the absorber layer in the photothermal trap. It has a hydrophobic surface, which makes it interesting for the vertical de-icing setup. Due to time limitations, a de-icing experiment that tested the de-icing time of 75/25 in a vertical setup was not done.

A de-icing setup conducted outside when the temperatures are below 0°C would also be of value, because of the stable temperatures that can be achieved. Furthermore, a focus on improving the experimental setup inside the styrofoam box would be beneficial.

For testing new materials, there are close to endless options, but a focus on materials that absorb light well is important. Growing carbon nanotubes could be interesting because of their properties regarding the absortion of light [31]. This is however a more expensive route to go.

Bibliography

[1] Olivier Parent and Adrian Ilinca. 'Anti-icing and de-icing techniques for wind turbines: Critical review'. In: *Cold Regions Science and Technology* 65.1 (Jan. 2011), pp. 88–96. DOI: 10.1016/j.coldregions.2010.01.005. URL: https://doi.org/10.1016/j.coldregions.2010.01.005.

[2] Husnu Yildirim Erbil. 'Improvement of lubricant-infused surfaces for anti-icing applications'. In: *Surface Innovations* 4.4 (Dec. 2016), pp. 214–217. DOI: 10.1680/jsuin.16.00026. URL: https://doi.org/10.1680/jsuin.16.00026.

[3] Sigifredo Castro, Lawrence C. Davis and Larry E. Erickson. 'Natural, cost-effective, and sustainable alternatives for treatment of aircraft deicing fluid waste'. In: *Environmental Progress* 24.1 (2005), pp. 26–33. DOI: 10.1002/ep.10059. URL: https://doi.org/10.1002/ep.10059.

[4] Susmita Dash, Jolet de Ruiter and Kripa K. Varanasi. 'Photothermal trap utilizing solar illumination for ice mitigation'. In: *Science Advances* 4.8 (Aug. 2018). DOI: 10.1126/sciadv.aat0127. URL: https://doi.org/10.1126/sciadv.aat0127.

[5] Vinod Upadhyay et al. 'Amphiphilic icephobic coatings'. In: *Progress in Organic Coatings* 112 (Nov. 2017), pp. 191–199. DOI: 10.1016/j.porgcoat.2017.07.019. URL: https://doi.org/10.1016/j.porgcoat.2017.07.019.

[6] Kripa K. Varanasi et al. 'Frost formation and ice adhesion on superhydrophobic surfaces'. In: *Applied Physics Letters* 97.23 (Dec. 2010), p. 234102. DOI: 10.1063/1.3524513. URL: https://doi.org/10.1063/1.3524513.

[7] Ann Kristin Lagmannsveen. 'De-icing coatings based on solar illumination Preparation and characterisation'. MA thesis. NTNU, 2020.

[8] Stine Sletvold. 'De-icing coatings based on solar illumination Preparation and characterization'. MA thesis. NTNU, 2022.

[9] Vahid Hejazi, Konstantin Sobolev and Michael Nosonovsky. 'From superhydrophobicity to icephobicity: forces and interaction analysis'. In: *Scientific Reports* 3.1 (July 2013). DOI: 10.1038/srep02194. URL: https://doi.org/10.1038/srep02194.

[10] Michael Nosonovsky and Vahid Hejazi. 'Why Superhydrophobic Surfaces Are Not Always Icephobic'. In: *ACS Nano* 6.10 (Sept. 2012), pp. 8488–8491. DOI: 10.1021/nn302138r. URL: https://doi.org/10.1021/nn302138r.

[11] Muhammad Imran Jamil et al. 'Slippery Photothermal Trap for Outstanding Deicing Surfaces'. In: *Journal of Bionic Engineering* 18.3 (May 2021), pp. 548–558. DOI: 10.1007/s42235-021-0046-7. URL: https://doi.org/10.1007/s42235-021-0046-7.

[12] Johannes Stemsrud. *De-Icing Coatings Based on Solar Illumination*. 2022.

[13] Carel Jan van Oss and Rossman F. Giese. 'Role of the Polar Properties of Water in Separation Methods'. In: *Separation &amp Purification Reviews* 40.3 (Aug. 2011), pp. 163–208. DOI: 10.1080/15422119.2011.555215. URL: https://doi.org/10.1080/15422119.2011.555215.

[14] Roger Hooke. 'Flow law for polycrystalline ice in glaciers: comparison of theoretical predictions, laboratory data, and field measurements. Rev Geophys Space Phys'. In: *Reviews of Geophysics* 19 (Jan. 1981), pp. 664–672.

[15] Masoud Farzaneh. *Atmospheric icing of power networks*. Springer Science & Business Media, 2008.

[16] Simen Ringdahl et al. 'Machine Learning Based Prediction of Nanoscale Ice Adhesion on Rough Surfaces'. In: *Coatings* 11.1 (Dec. 2020), p. 33. DOI: 10.3390/coatings11010033. URL: https://doi.org/10.3390/coatings11010033.

[17] Liangliang Cao et al. 'Anti-icing superhydrophobic coatings'. In: *Langmuir* 25.21 (2009), pp. 12444–12448.

[18] Zhongliang Liu et al. 'Frost formation on a super-hydrophobic surface under natural convection conditions'. In: *International Journal of Heat and Mass Transfer* 51.25-26 (2008), pp. 5975–5982.

[19] Stefan Jung et al. 'Are Superhydrophobic Surfaces Best for Icephobicity?' In: *Langmuir* 27.6 (Feb. 2011), pp. 3059–3066. DOI: 10.1021/la104762g. URL: https://doi.org/10.1021/la104762g.

[20] Jean-Denis Brassard et al. 'Icephobicity: Definition and measurement regarding atmospheric icing'. In: *Contamination mitigating polymeric coatings for extreme environments* (2019), pp. 123–143.

[21] C.J. Van Oss et al. 'Surface tension parameters of ice obtained from contact angle data and from positive and negative particle adhesion to advancing freezing fronts'. In: *Journal of Adhesion Science and Technology* 6.4 (Jan. 1992), pp. 503–516. DOI: 10.1163/156856192x00827. URL: https://doi.org/10.1163/156856192x00827.

[22] Muhammad Imran Jamil et al. 'Icephobic Strategies and Materials with Superwettability: Design Principles and Mechanism'. In: *Langmuir* 34.50 (Nov. 2018), pp. 15425–15444. ISSN: 1520-5827. DOI: 10.1021/acs.langmuir.8b03276. URL: http://dx.doi.org/10.1021/acs.langmuir.8b03276.

[23] A. B. D. Cassie and S. Baxter. 'Wettability of porous surfaces'. In: *Transactions of the Faraday Society* 40 (1944), p. 546. ISSN: 0014-7672. DOI: 10.1039/tf9444000546. URL: http://dx.doi.org/10.1039/tf9444000546.

[24] N.X. Randall, G. Favaro and C.H. Frankel. 'The effect of intrinsic parameters on the critical load as measured with the scratch test method'. In: *Surface and Coatings Technology* 137.2-3 (Mar. 2001), pp. 146–151. DOI: 10.1016/s0257-8972(00)01097-5. URL: https://doi.org/10.1016/s0257-8972(00)01097-5.

[25] J.C. WILLIAMS. 'Doctor-Blade Process'. In: *Treatise on Materials Science &amp Technology*. Elsevier, 1976, pp. 173–198. DOI: 10.1016/b978-0-12-341809-8.50016-4. URL: https://doi.org/10.1016/b978-0-12-341809-8.50016-4.

[26] E.-K Raasok. 'Hydrophobic Coatings for Anti-Icing Applications'. MA thesis. NTNU, 2014.

[27] Hoon Joo Lee. 'Design and development of anti-icing textile surfaces'. In: *Journal of Materials Science* 47.13 (Mar. 2012), pp. 5114–5120. DOI: 10.1007/s10853-012-6386-2. URL: https://doi.org/10.1007/s10853-012-6386-2.

[28] Noor Al-Huda Al-Aaraji et al. 'Synthesis and Enhanced Optical Characteristics of Silicon Carbide/Copper Oxide Nanostructures Doped Transparent Polymer for Optics and Photonics Nanodevices'. In: *Silicon* 14.15 (Feb. 2022), pp. 10037–10044. DOI: 10.1007/s12633-022-01730-7. URL: https://doi.org/10.1007/s12633-022-01730-7.

[29] Rafael Kenji Nishihora et al. 'Manufacturing porous ceramic materials by tape casting—A review'. In: *Journal of the European Ceramic Society* 38.4 (Apr. 2018), pp. 988–1001. DOI: 10.1016/j.jeurceramsoc.2017.11.047. URL: https://doi.org/10.1016/j.jeurceramsoc.2017.11.047.

[30] M. Jabbari et al. 'Ceramic tape casting: A review of current methods and trends with emphasis on rheological behaviour and flow analysis'. In: *Materials Science and Engineering: B* 212 (Oct. 2016), pp. 39–61. DOI: 10.1016/j.mseb.2016.07.011. URL: https://doi.org/10.1016/j.mseb.2016.07.011.

[31] K.S. Pandya and N.K. Naik. 'Energy absorption capability of carbon nanotubes dispersed in resins under compressive high strain rate loading'. In: *Composites Part B: Engineering* 72 (Apr. 2015), pp. 40–44. DOI: 10.1016/j.compositesb.2014.11.026. URL: https://doi.org/10.1016/j.compositesb.2014.11.026.

Appendix

A De-icing experiments

Images of de-icing experiments done to map the temperature distribution of the styrofoam box is presented.

Figure .1, Figure .3 and Figure .2 shows three images of experiments done to map the temperature distribution inside the styrofoam box, and to get a better understanding of how to conduct future de-icing experiments.
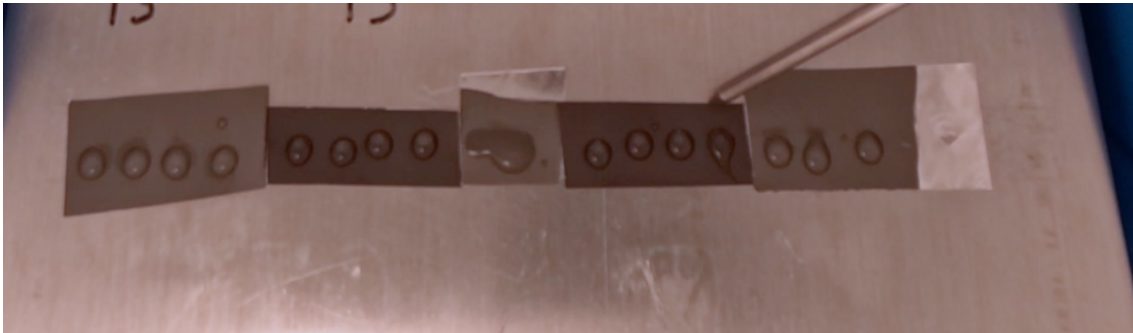

Figure .1: Two prototypes, namely the SiC in gray and the 50/50 in black were used. The droplets have all melted.
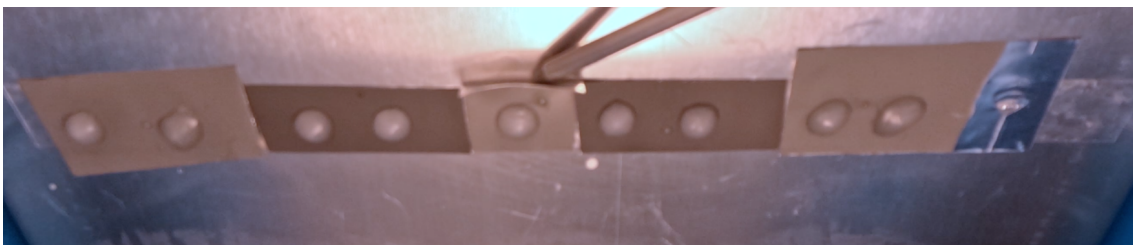

Figure .2: Two prototypes, namely the SiC and the 50/50 prototypes was used.
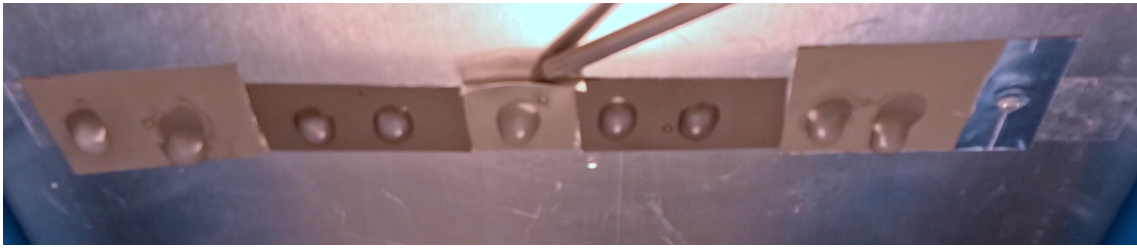
Figure .3: Two prototypes, namely the SiC and the 50/50 prototypes was used. Hear with frozen droplets ontop.